Stratified Kolmogorov flow

By N E I L J. B A L M F O R T H[1] and Y U A N - N A N Y O U N G[2]

[1]Department of Applied Mathematics and Statistics, University of California,
Santa Cruz, CA 95064, USA

[2]Department of Engineering Sciences and Applied Mathematics, Northwestern University,
Evanston, IL 60208, USA

In this study we investigate the Kolmogorov flow (a shear flow with a sinusoidal velocity profile) in a weakly stratified, two-dimensional fluid. We derive amplitude equations for this system in the neighbourhood of the initial bifurcation to instability for both low and high Péclet numbers (strong and weak thermal diffusion, respectively). We solve amplitude equations numerically and find that, for low Péclet number, the stratification halts the cascade of energy from small to large scales at an intermediate wavenumber. For high Péclet number, we discover diffusively spreading, thermal boundary layers in which the stratification temporarily impedes, but does not saturate, the growth of the instability; the instability eventually mixes the temperature inside the boundary layers, so releasing itself from the stabilizing stratification there, and thereby grows more quickly. We solve the governing fluid equations numerically to compare with the asymptotic results, and to extend the exploration well beyond onset. We find that the arrest of the inverse cascade by stratification is a robust feature of the system, occurring at higher Reynolds, Richards and Péclet numbers – the flow patterns are invariably smaller than the domain size. At higher Péclet number, though the system creates slender regions in which the temperature gradient is concentrated within a more homogeneous background, there are no signs of the horizontally mixed layers separated by diffusive interfaces familiar from doubly diffusive systems.

1. Introduction

The stability of viscous shear flows is a notoriously difficult problem that has occupied fluid dynamicists for more than a century. Without the effects of stratification and compressibility, the linear theory of the problem is based on the solution of the Orr–Sommerfeld equation. Few general results and exact solutions are known for this equation. A notable exception is the so-called Kolmogorov flow, first studied by Meshalkin & Sinai (1961), for which the eigenvalue problem can be reduced to a study of some continued fractions (Friedlander & Howard 1998). Kolmogorov flow is a two-dimensional, unidirectional shear flow with a sinusoid velocity profile ($U = \sin z$, where z is the cross-stream coordinate) which, in viscous fluid, must be maintained by an external forcing. Because of its simplicity and accessibility to analysis, Kolmogorov advocated this flow as a theoretical laboratory in which to study fluid instability and the transition to turbulence. Forced electrolytic fluids (Bondarenko, Gak & Dolzhansky 1979; Batchayev 1988), and driven soap films (Burgess *et al.* 1999) have also provided experimental realizations of the flow.

Many previous theoretical studies have focused on deriving the critical Reynolds number for the onset of instability in unstratified Kolmogorov flows (Meshalkin &

Sinai 1961; Beaumont 1981; Thess 1992; Murakami & Watanabe 1994), and amplitude equations describing the resulting pattern formation (Nepomniashchii 1976; Sivashinsky 1985). These studies have been extended into more strongly unstable regimes with numerical simulation (Nicolaenko & She 1989; Platt, Sirovich & Fitzmaurice 1991; Armbruster *et al.* 1992). Notably, it was found that small-scale instabilities create a negative effective viscosity which seeds a cascade of energy from the injection scale (the lengthscale of the sinusoidal basic flow) to the largest spatial scales. Hence, the configuration provides a simple visualization of one of the ingredients of two-dimensional turbulence (Green 1974). Generalization of the Kolmogorov basic state (Beloshapkin *et al.* 1989) also illustrates the formation of a wide variety of patterns with symmetries of crystals and quasi-crystals.

Kolmogorov flows have also been studied in geophysical fluid dynamics with regard to the stability of finite-amplitude Rossby waves in the atmosphere (Lorenz 1972) and to gauge whether small-scale forcing such as baroclinic instability can cascade into planetary-scale flows (Manfroi & Young 1999). These studies also add two further physical effects to the Kolmogorov flow: the beta effect (the planetary vorticity gradient) and (bottom) friction. A major qualitative change introduced by those physical effects is the arrest of the inverse cascade; energy is no longer channelled to the longest wavelengths, but builds up over intermediate lengthscales (Frisch, Legras & Villone 1996; Manfroi & Young 1999; Legras, Villone & Frisch 1999).

In this study we continue to mine the vein suggested by Kolmogorov. Specifically, we add gravity in the direction transverse to the Kolmogorov flow and explore how weak stratification modifies the basic linear instability and its nonlinear development. Because stratification exerts a large-scale stabilizing influence, here too we anticipate an arrest of the inverse cascade. Again, there are some geophysical motivations, such as the stability of vertical shear flows of the atmosphere (Davis & Peltier 1976) and of internal gravity waves with finite amplitude (Kurgansky 1980). Stratified Kolmogorov flows have also been created in the laboratory (Batchayev, Dovzhenko & Kurgansky 1984; Batchayev & Kurgansky 1986). However, we will not directly consider these applications, and describe only the fluid mechanical problem. A preliminary report on this work can be found in Young (1999).

The paper is structured as follows. First, we analyse the linear stability of stratified Kolmogorov flow. We then delve into weakly nonlinear, long-wave theory for the instability. Two particular physical regimes must be dealt with. In §4, we consider weakly stratified flows in which heat diffuses relatively quickly compared to the unfolding time of the instability. This case has many similarities with long-wave instability for non-stratified flows, and we base the amplitude expansion on Sivashinsky's earlier effort. When thermal diffusion is relatively slow, however, we encounter a different physical regime in which sharp, internal, thermal boundary layers can develop in the temperature field. This case is considered in §5. Finally, in §6, we present results from direct numerical simulations of the governing equations to complement and extend the asymptotic analyses.

2. Formulation

We start with the vorticity and heat equations for two-dimensional stratified flow in the Boussinesq approximation. The flow is defined on the (x, z)-plane with gravity g directed along $-z$. We exploit the incompressibility of the velocity field to express the velocity components in terms of a streamfunction, $\Psi(x, z, t)$. The background Kolmogorov shear flow is characterized by $\Psi_0 = U_0 l \cos(z/l)$, where U_0 is the ampli-

tude and $2\pi l$ is the periodicity of the shear flow. The stabilizing linear temperature variation of the background is $T_0 = (\Delta T/l)z$, where ΔT is the temperature difference across a height l.

We separate the streamfunction and temperature of an evolving disturbance from the basic state, and use l, U_0 and l/U_0 to remove the dimensions from the governing equations. That is, we set $\Psi = \Psi_0 + U_0 l \psi(x, z, t)$ and $T = T_0 + \Delta T \, \theta(x, z, t)$, and write the dimensionless vorticity and heat equations,

$$\partial_t \nabla^2 \psi - (\nabla^2 \psi + \psi)_x \sin z - J(\psi, \nabla^2 \psi) = \frac{1}{Re} \nabla^4 \psi - Ri\theta_x \tag{2.1}$$

and

$$\partial_t \theta - \theta_x \sin z - \psi_x - J(\psi, \theta) = \frac{1}{Pe} \nabla^2 \theta. \tag{2.2}$$

A number of dimensionless numbers appear: $Re \equiv U_0 l/v$ is the Reynolds number, $Pe \equiv U_0 l/\kappa$ is the Péclet number, and $Ri \equiv g\alpha\Delta T l/U_0^2$ is the Richardson number. The dimensionless basic state is a shear flow with profile $u_0 = -\sin z$ and unit temperature gradient.

We solve the equations on a periodic domain, $x \in [0, L_x]$ and $z \in [0, L_z]$. In principle, perturbations need not have the same (vertical) periodicity as the basic flow, and so L_z is not necessarily 2π. However, computations for the unstratified linear stability problem (Beaumont 1981, Friedlander & Howard 1998), supplemented with some of our own for the stratified case, suggest that the most unstable mode always has the same periodicity as the basic flow profile. We therefore set most of our exploration in domains with $L_z = 2\pi$; at the very end of our study we consider a more extensive basic flow with $L_z = 16\pi$. Except in particular examples, the horizontal domain size L_x is left arbitrary (large horizontal domains, with $L_x \gg 1$ will be of most interest).

The dimensionless equations are formulated in such a way as to recover the unstratified Kolmogorov problem if $Ri = 0$. Consequently, the Péclet number appears in the heat equation, and the more customary Prandtl number, $Pr = v/\kappa$, is not used. It is useful to recall that $Pe = PrRe$ and $Ra = RiRe^2Pr$, where Ra is the Rayleigh number.

3. Linear stability theory

We first present results for the linear stability of the basic state: we drop the non-linear terms and look for normal modes with dependence, $[\psi, \theta] = e^{ik(x-ct)}[\hat{\psi}(z), \hat{\theta}(z)]$, where $\hat{\psi}(z)$ and $\hat{\theta}(z)$ are periodic functions on $[0, 2\pi]$. Then,

$$\frac{1}{ikRe}\left(\frac{d^2}{dz^2} - k^2\right)^2 \hat{\psi} + (c + \sin z)\left(\frac{d^2}{dz^2} - k^2\right)\hat{\psi} + \hat{\psi}\sin z - Ri\hat{\theta} = 0 \tag{3.1}$$

and

$$\frac{1}{ikPe}\left(\frac{d^2}{dz^2} - k^2\right)\hat{\theta} + (c + \sin z)\hat{\theta} + \hat{\psi} = 0. \tag{3.2}$$

When $Ri = 0$, the normal-mode problem reduces to that studied previously, and can be reduced to the consideration of a continued fraction (Friedlander & Howard 1998). The critical Reynolds number is $Re_c = \sqrt{2}$, and just beyond this threshold the

flow is unstable to waves with small horizontal wavenumber, $k \ll 1$, and growth rate,

$$s = -\mathrm{i}kc = \frac{1}{Re}(Re^2 - 2)k^2 - Re\left(1 + \frac{Re^2}{4}\right)k^4 + O(k^6). \tag{3.3}$$

In sections to come we generalize this formula to capture effects of weak stratification, but first we give more details of the linear stability.

3.1. *Ideal limit*

In the ideal limit, $Re \to \infty$ and $Pe \to \infty$, and the equations are simplified by virtue of the leading spatial derivatives disappearing from the problem. The simplified equations can be combined into the Taylor–Goldstein equation,

$$\psi'' - k^2\psi + \frac{\psi \sin z}{c + \sin z} + \frac{Ri\,\psi}{(c + \sin z)^2} = 0. \tag{3.4}$$

From this equation we may derive the celebrated Richardson number criterion: instability can only occur provided $Ri < 1/4$ (Drazin & Howard 1996). However, a major complication over the viscous and diffusive problem is that the eigenvalue equation is singular at the critical levels, where $c = U \equiv -\sin z$. As a result, the eigenvalues form a continuous spectrum for all neutral waves that have critical levels (Case 1960). Fortunately, the modes responsible for instability have discrete eigenvalues, and so normal-mode methods may be used to detect them.

In the case at hand, we find a class of stationary neutral solutions with $c = 0$ by rewriting the equation in the form

$$\left(\frac{\mathrm{d}^2}{\mathrm{d}z^2} + 1 - k^2 + \frac{Ri}{\sin^2 z}\right)\psi = \left(\frac{\mathrm{d}}{\mathrm{d}z} + \sqrt{1 - k^2}\cot z\right)\left(\frac{\mathrm{d}}{\mathrm{d}z} - \sqrt{1 - k^2}\cot z\right)\psi = 0, \tag{3.5}$$

where

$$Ri = \sqrt{1 - k^2} - (1 - k^2). \tag{3.6}$$

By virtue of the factorization in (3.5), we find the two independent solutions

$$\psi_1 = (\sin z)^{\sqrt{1-k^2}} \tag{3.7}$$

and

$$\psi_2 = (\sin z)^{\sqrt{1-k^2}} \int^z (\sin z')^{-2\sqrt{1-k^2}}\mathrm{d}z'. \tag{3.8}$$

The two solutions are not regular functions and require interpretation when $\sin z < 0$. This mirrors Holmboe's solution for a mixing layer profile. For that shear flow, continuation from unstable wavenumbers can be used to select the correct branch of the multi-valued function analogous to $(\sin z)^{\sqrt{1-k^2}}$ (Howard 1963). Here, a similar procedure predicts that ψ_1 is the limiting neutral mode of a branch of unstable modes and we should take $\psi_1 = |\sin z|^{\sqrt{1-k^2}}$. ($\psi_2$ appears to be non-periodic.)

The Richardson number defined by (3.6) is plotted as a function of k in figure 1. The curve has a maximum value of $1/4$ when $k = \sqrt{3}/2$. Howard's version of the Tollmien–Lin perturbation calculation (Howard 1963) indicates that there is an unstable mode below this curve, in agreement with the numerical solutions of the eigenvalue problem that are also included in the figure. The curve therefore appears to be the true stability boundary, and the Richardson number criterion, $Ri < 1/4$, is sufficient for instability.
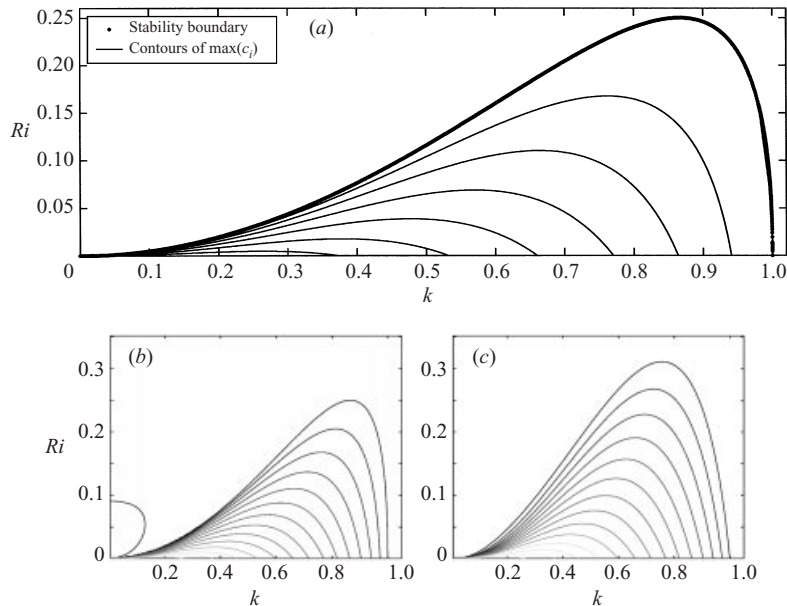
FIGURE 1. (*a*) Stability boundary for the inviscid, non-diffusive limit. Also shown are contours of constant max(c_i), at levels of multiples of 0.1. (*b*, *c*) Corresponding pictures for weakly viscous and diffusive flows (with $Re = 10^{-4}$ and $Pe = 10^{-5}$, and $Re = 10^{-5}$ and $Pe = 1$, respectively), in steps of 0.05 for max(c_i).

3.2. *Viscous flows*

For viscous flows, we solve the eigenvalue problem numerically. Maximal values of c_i are shown in figure 1(*b*, *c*). These pictures largely confirm that the ideal instability is qualitatively unchanged by the dissipation. However, somewhat surprisingly, there are parameter regimes in which the instability extends to $Ri > 1/4$ when diffusion is included. This feature probably has some analogy with the diffusive destabilization of vortices (McIntyre 1970).

Figure 2 shows curves of neutral stability on the (k, Re)-plane for weakly stratified flows. The curves are invariably confined to the wavenumber range $0 \leqslant k \leqslant 1$. From data of this kind, we identify the critical wavenumbers and Reynolds numbers. These are plotted in figure 3 as functions of Richardson numbers for Prandtl number $Pr \equiv \nu/\kappa = 10$ (so $Pe = 10Re$). (As a prelude to the asymptotic analysis to come shortly, the results from long-wave expansions are included in figure 3.)

As shown in the figures, the critical Reynolds number, Re_c, and wavenumber, k_c, increase with increasing Richardson number. We can uncover both these trends analytically by performing a long-wave expansion about the critical Reynolds number for weakly stratified flows. The goal of the next two sections is to derive that long-wave theory. We need two expansions because there are two possible limits for the thermal diffusivity: when Pe is not large, thermal diffusion is relatively rapid relative to the growth of the instability and the temperature field relaxes almost instantaneously. However, if $Pe \gg 1$, thermal relaxation can be as slow or slower than the instability, leading to a very different kind of dynamical behaviour.

The second case is significantly more complicated, as foreshadowed by the singularity that appears in the linear stability problem when $Pe \to \infty$: in this limit,
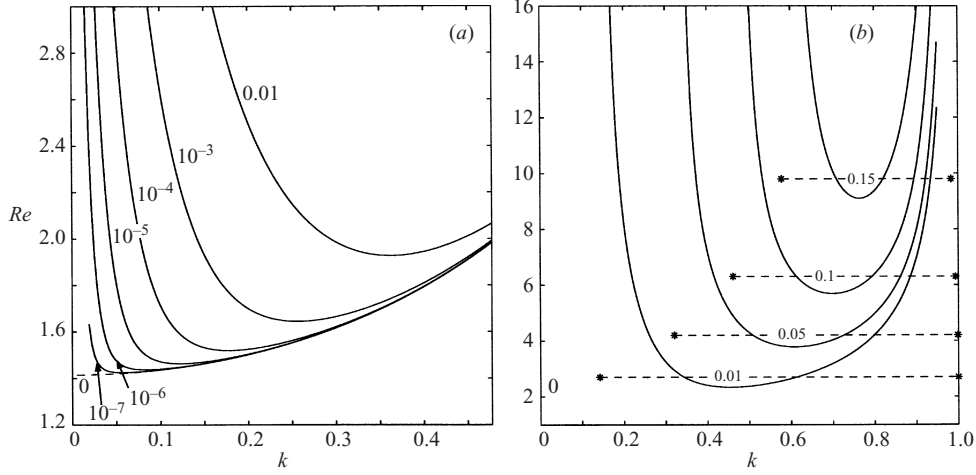
FIGURE 2. Stability boundaries on the (k, Re)-plane for weakly stratified flow with Prandtl number $Pr = 1$. Curves are labelled by the Richardson number: (a) $Ri = 10^{-7}$, 10^{-6}, 10^{-5}, 10^{-4}, 10^{-3}, and 10^{-2}; (b) $Ri = 0.01$, 0.05, 0.1 and 0.15. In (b), the wavenumber ranges for inviscid instabilities are also shown.
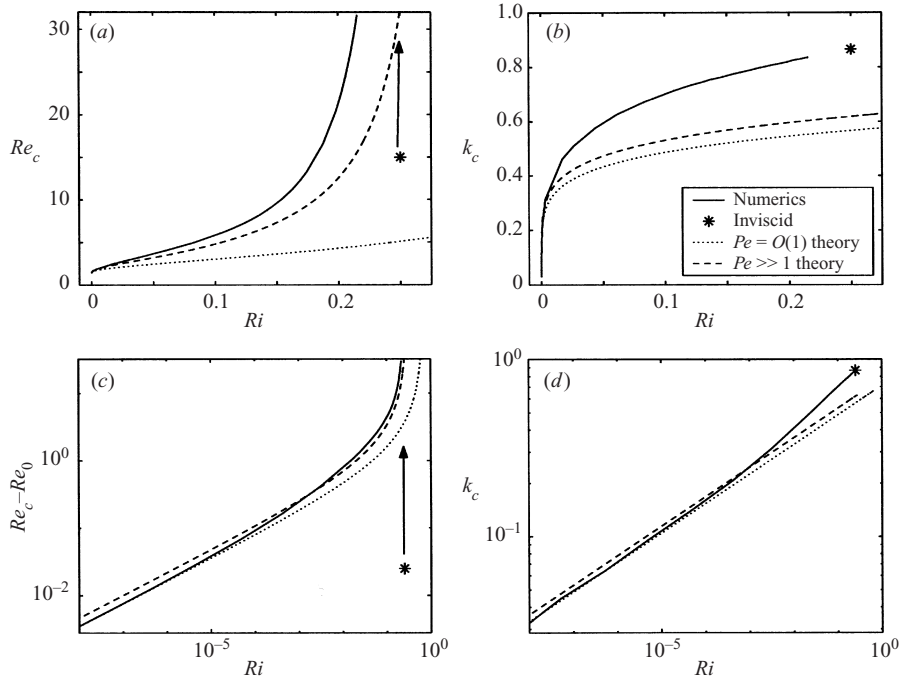

FIGURE 3. Critical Reynolds number (a) and critical wavenumber (b) as functions of Richardson number for $Pr = 10$ for the periodic case. (c, d) The data on logarithmic plots. The inviscid marginal stability point, $k_c = \sqrt{3}/2$ and $Ri = 1/4$ as $Re \to \infty$ is shown, together with curves constructed using the long-wave analyses.

$\hat{\theta} \to -\hat{\psi}/(c + \sin z)$ and the eigenvalue equation becomes

$$\frac{1}{ikRe} \left(\frac{\mathrm{d}^2}{\mathrm{d}z^2} - k^2 \right)^2 \hat{\psi} + (c + \sin z) \left(\frac{\mathrm{d}^2}{\mathrm{d}z^2} - k^2 \right) \hat{\psi} + \hat{\psi} \sin z + \frac{Ri\hat{\psi}}{c + \sin z} = 0. \quad (3.9)$$
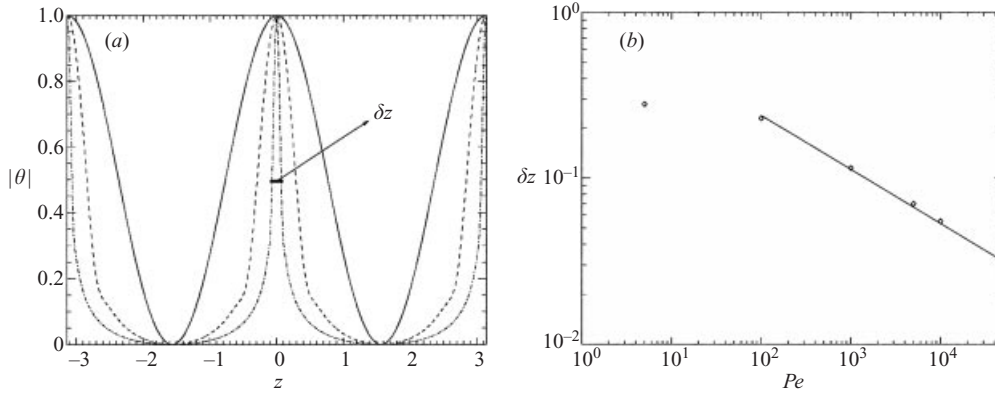
FIGURE 4. (*a*) Development of internal boundary layer structure in the temperature eigenfunction $\theta(z)$ of the neutral mode as we increase the Péclet number for $Re = 1.92$ and $Ri = 0.01$. Solid, dashed, and dash-dotted lines are, respectively, $Pe = 20$, 2×10^3, and 2×10^5. (*b*) Boundary layer thickness (δz, as defined in (*a*)) as a function of Pe. The solid line is the best fit for the last five points, $\delta z \sim Pe^{-0.326}$, which is in agreement with simple dimensional analysis which predicts $\delta z \sim Pe^{1/3}$. (NB because the neutral modes have order unity wavenumber, this scaling is different from the long-wave theory of §5).

The critical-level-like singularity for $c = -\sin z$ reflects a continuous spectrum of eigenvalues describing re-arrangements of the temperature field. If $Ri \ll 1$, we may treat the stratification term perturbatively, in which case we find an eigenvalue correction,

$$\delta c = -Ri \frac{\displaystyle\int_0^{2\pi} \hat{\varphi}^\dagger \hat{\varphi} \, \mathrm{d}z / (c + \sin z)}{\displaystyle\int_0^{2\pi} \hat{\varphi}^\dagger (\hat{\varphi}'' - k^2 \hat{\varphi}) \, \mathrm{d}z}, \tag{3.10}$$

where $\hat{\varphi}^\dagger$ is the adjoint eigenfunction. The right-hand side of this expression contains a singular integral much like that encountered in conventional Tollmien–Lin perturbation theory. Importantly, as in that theory, the eigenvalue correction is predicted to have different limits as $c_i \to 0$ from either above or below (we explicitly observe this discontinuous behaviour in §5).

Further complications appear in the nonlinear theory, which as a consequence proceeds by way of matched asymptotics similar to standard critical-layer theory (Warn & Warn 1978, Stewartson 1981). The matched asymptotics are needed because the singularities of the linear theory must be removed within narrow boundary layers surrounding the singular levels. The development of these thermal boundary layers can be seen in the linear eigenfunction $\hat{\theta}(z)$ as we approach the diffusionless limit (figure 4).

4. Weak instability for $Pe \sim O(1)$

4.1. *Long-wave expansion*

In this section we construct the long-wave amplitude equation for $Pe \sim O(1)$. The aim is to generalize Sivashinky's long-wave expansion (Sivashinsky 1985) to weakly stratified flows; the analysis is very similar and we relegate the details to Appendix A.

To focus on the weakly stratified limit, we rescale the Richardson number $Ri \equiv \epsilon^6 Ri_6$, and, to expand about the critical Reynolds number, we set $Re = \sqrt{2}/(1-\epsilon^2)$. We
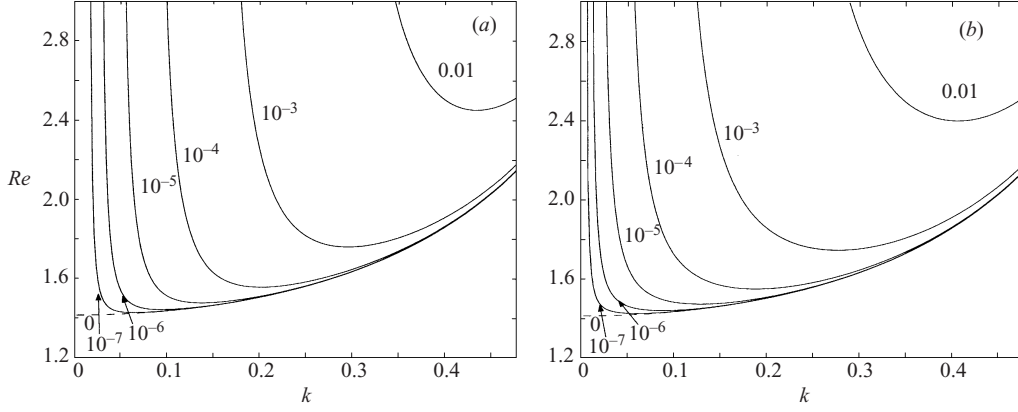
FIGURE 5. Stability boundaries on the (k, Re)-plane predicted by long-wave theory for $Pr = 1$. Curves are labelled by the Richardson number. The long-wave theory for (a) order unity Péclet numbers and (b) the large Péclet number theory (§ 5).

further introduce the long-wave coordinate, $\xi = x/\epsilon$, and a slow timescale, $\tau = t/\epsilon^4$. The precise scalings are dictated by a distinguished limit of the parameters of the problem, and are evident in the amplitude equations that we eventually derive:

$$A_{\xi\xi\tau} + \frac{3\sqrt{2}}{2} A_{\xi\xi\xi\xi\xi\xi} + \sqrt{2} \left[\left(1 - \tfrac{2}{3}A_\xi^2 \right) A_\xi \right]_{\xi\xi\xi} = \frac{2PeRi_6}{Pe^2 + 2}(A - \langle A \rangle). \quad (4.1)$$

Here, $A(\xi, \tau)$ denotes the leading-order streamfunction, and the angular brackets denote horizontal average.

A linearization of the amplitude equation about $A = 0$ allows us to reconsider the linear stability of the weakly stratified flow: let $A \sim \exp(i\epsilon k\xi + \epsilon^4 s\tau) \equiv \exp(ikx + st)$. Then,

$$s = \sqrt{2}\left(1 - \frac{\sqrt{2}}{Re} \right) k^2 - \frac{3}{\sqrt{2}}k^4 - \frac{2PeRi_6}{(Pe^2 + 2)k^2} + O(\epsilon^4 k^2), \quad (4.2)$$

on recalling the definition of ϵ^2, which reveals the stabilizing influence of stratification on long waves. This approximation leads to the stability boundaries shown in figure 5, which should be compared with figure 2(a). (Also displayed are parallel results for the $Pe \gg 1$ theory of § 5.)

4.2. Canonization and dynamics

A simple rescaling places the long-wave equation into a canonical form containing a single parameter λ:

$$G_\tau + G_{\xi\xi} + G_{\xi\xi\xi\xi} - (G^3)_{\xi\xi} = \lambda H, \quad H_{\xi\xi} = G, \quad (4.3)$$

with $G \propto (A - \langle A \rangle)_\xi$ and $\lambda = 9\sqrt{2}PeRi_6/(2 + Pe^2)$; the size of the domain, d, in which we solve this equation is a further parameter. The canonized form highlights the connection with the Cahn–Hilliard equation (Sivashinsky 1985; Chapman & Proctor 1980, and its variants (Manfroi & Young 1999; Legras *et al.* 1999). In view of the diagnostic form of the function H, there is a resemblance to KP equations.

The system (4.3) has a Lyapunov functional,

$$\mathscr{F}[G] \equiv \int_0^d (\tfrac{1}{4}G^4 - \tfrac{1}{2}G^2 + \tfrac{1}{2}G_\xi^2 + \tfrac{1}{2}\lambda H^2)\,d\xi, \quad (4.4)$$
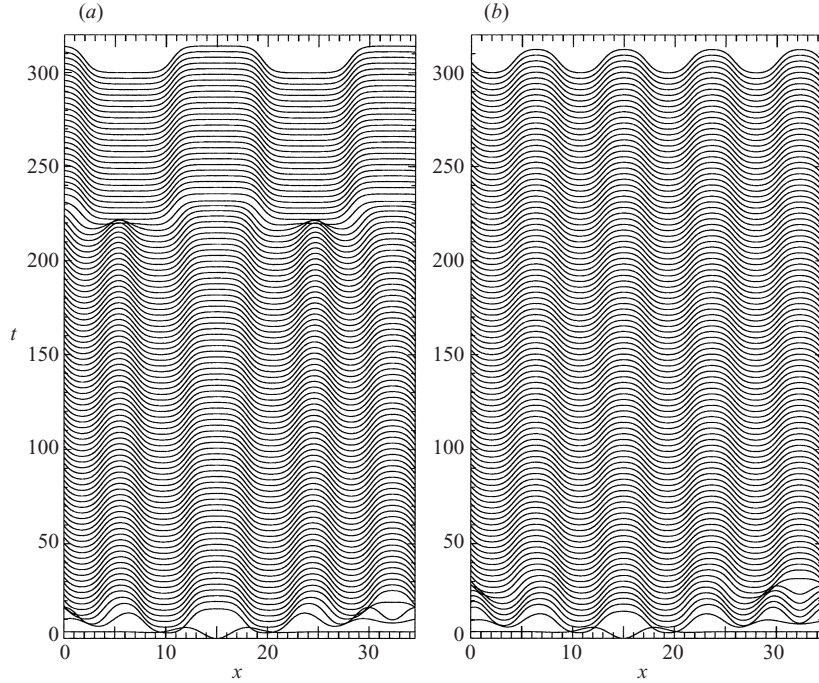
FIGURE 6. Time–space plots of the amplitude gradient with (*a*) $Ri_6 = 0$ and (*b*) $Ri_6 = 0.1$, with $Pe = 1$. The scale of the time axis also shows the amplitude scale. This plot shows the solutions for the unscaled variable $A_\xi(\xi, T)$, as found numerically using a pseudo-spectral code.

for which

$$\frac{\mathrm{d}\mathscr{F}}{\mathrm{d}\tau} = -\int_0^d H_\tau^2 \mathrm{d}\xi \leqslant 0. \tag{4.5}$$

Therefore, because $\mathscr{F}[G]$ must decay in time to a minimal value, and because any minimum of $\mathscr{F}[G]$ is equivalent to a steady solution of (4.3), the system must approach a stationary state from an arbitrary initial condition.

The steady solutions, $G(\xi) = g(\xi)$ and $H = h(\xi)$, satisfy

$$g_{\xi\xi} + g_{\xi\xi\xi\xi} - (g^3)_{\xi\xi} = \lambda h, \quad g = h_{\xi\xi}. \tag{4.6}$$

Provided $d > 2\pi$, and depending on the value of λ, these equations have non-trivial solutions. One variety of such solutions can be regarded as 'pure modes' which, on treating either d or λ as a control parameter, bifurcate from the trivial state $g = 0$. At the points of bifurcation, these modes have a sinusoidal form, $g = \sin(n\pi\xi/d)$, given by a particular integer n, and we may index them accordingly. In addition to the pure modes, secondary bifurcations may lead to 'mixed modes' that connect the different pure-mode solution branches.

For $\lambda = 0$, the only stable steady equilibrium is that with longest wavelength, the $n = 1$ pure mode (Chapman & Proctor 1980), and there are no secondary bifurcations and mixed modes. The system must therefore progress inexorably to the largest-scale steady equilibrium even when there may be more unstable normal modes with shorter scale. This is the essence of the inverse cascade in the unstratified problem. However, the passage to the final state can be very protracted, as illustrated in figure 6(*a*). This figure shows the initial evolution of $G(\xi, \tau)$ from a low-amplitude, random initial
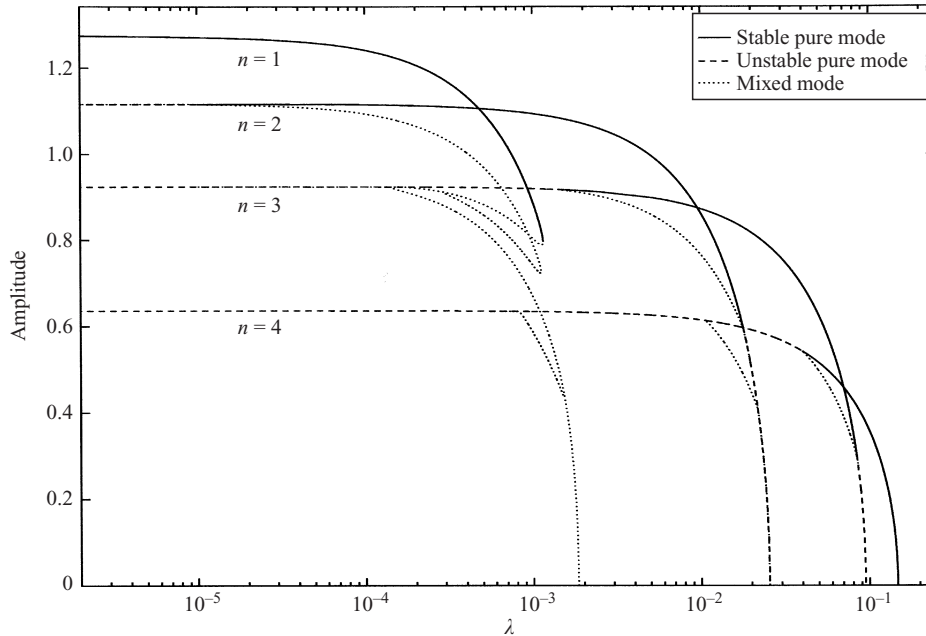
FIGURE 7. Bifurcation diagram for $d = 30$: the amplitude measure, $(\langle g^2 \rangle)^{1/2}$, against the rescaled Richardson number λ.

condition. The system first rapidly forms a sequence of interfaces separating almost homogeneous 'phases' (in the gradient $G(\xi, \tau)$). Certain interfaces then slowly drift toward one another, eventually precipitating sudden interface collisions wherein two of the homogeneous phases disappear. This dynamics repeats over a longer timescale than is shown, and the collisions gradually coarsen the pattern and eliminate the interfaces. Ultimately, only the largest-scale state remains with a single pair of interfaces (this is the $n = 1$ pure mode). Such coarsening is the usual phenomenology associated with the Cahn–Hilliard equation; here it corresponds to slowly evolving patterns of vortices interrupted by rapid mergers (She 1987).

When $\lambda \neq 0$, the bifurcations of the equilibrium solutions are different: mixed modes now appear that destabilize the $n = 1$ mode, then connect to and stabilize the pure modes with $n > 1$. A sample bifurcation diagram for $d = 30$ and varying λ is illustrated in figure 7, and the variety of pure modes and their ranges of stability for $d = 12\pi$ are shown in figure 8. Evidently, shorter-scale multiple equilibria appear instead of the gravest mode, and so there is no longer any reason to expect a complete inverse cascade. Indeed, numerical solutions of the amplitude equation with $\lambda \neq 0$ display the arrest of the cascade for patterns of intermediate scale – see figure 6(b). Here, there is a single collision and the state with eight interfaces (the $n = 4$ pure mode – see figure 8) persists indefinitely. This modification of the Cahn–Hilliard dynamics is similar to that observed in Kolmogorov flow on the beta-plane and with friction (Frisch *et al.* 1996; Manfroi & Young 1999).

5. Weak instability for $Pe \gg 1$

In many physical systems (salty water, for example), the Péclet number for a Reynolds number of $\sqrt{2}$ is of the order of 1000. Thus, cases where $Pe \gg 1$ can be
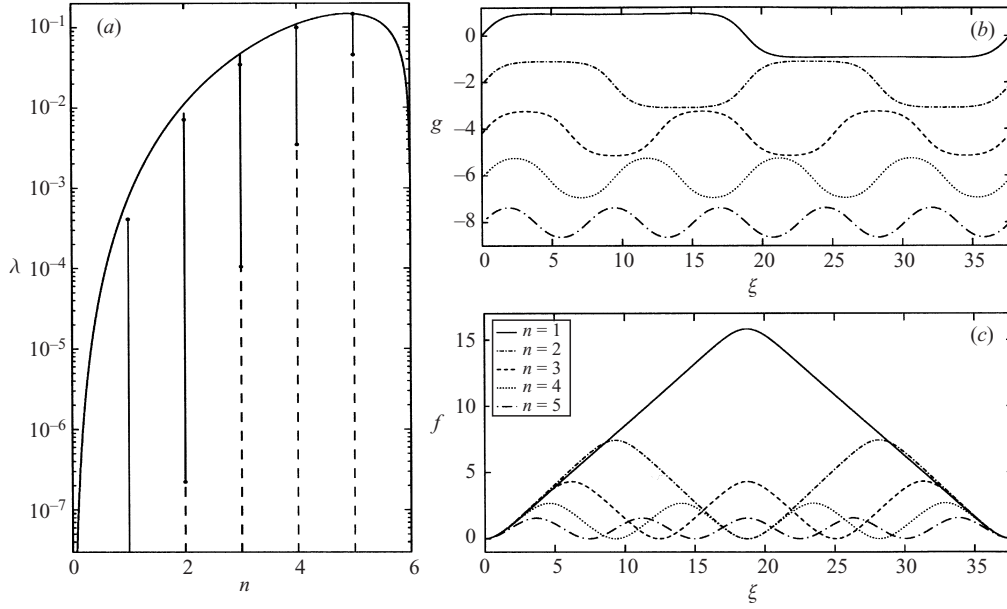
FIGURE 8. Numerically computed pure-mode solutions. (*a*) The ranges of λ over which the pure modes with $n = 1 - 5$ exist (below curve) and are stable (solid sections of vertical lines). (*b,c*) The shapes of these solutions for $\lambda = 10^{-4}$; (*b*) shows g and (*c*) shows f, the integral of g (the streamfunction). $d = 12\pi$.

physically relevant, and we now focus on this weakly diffusive limit. As before, we set

$$Ri = \epsilon^5 Ri_5, \quad \partial_t = \epsilon^4 \partial_\tau, \quad \partial_x = \epsilon \partial_\xi. \tag{5.1}$$

We also now add the scalings

$$Pe = \epsilon^{-10} Pe_{10}, \quad \psi = \epsilon^6 \phi, \quad \theta = \epsilon^6 \vartheta. \tag{5.2}$$

The first ensures a weakly diffusive limit. The latter pair is necessary because the amplitude at which nonlinearity comes into play is much reduced compared to the diffusive case as a result of the presence of near-singular boundary layers: in §3, we pointed out that, for $Pe \to \infty$, critical-level-like singularities appear in the linear eigenvalue problem. In the nonlinear theory, these singularities become regularized within thermal boundary layers on using matched asymptotic expansion, but the amplitude of the disturbance remains relatively large over these special regions, promoting nonlinear effects there.

The technical details of the expansion are relegated to Appendix B; we quote only the final result:

$$A_{\tau\xi} + \frac{3}{\sqrt{2}} A_{\xi\xi\xi\xi\xi} + \sqrt{2} A_{\xi\xi\xi} = -\frac{Ri_5}{\pi} \int_{-\infty}^{\infty} \Theta \, dZ, \tag{5.3}$$

$$\Theta_\tau + Z\Theta_\xi + A_\xi \Theta_Z - A_\xi = \mu\Theta_{ZZ}, \tag{5.4}$$

where $\mu = 1/Pe_{10}$, $A(\xi, \tau)$ is again the leading-order (global) streamfunction, $\Theta(\xi, Z, \tau)$ denotes the temperature fluctuation inside the boundary layers (by a symmetry of the problem, the thermal disturbance is identical inside each boundary layer), which have an expanded vertical coordinate Z resolving them, and which cover infinite intervals in the asymptotic scheme. This system has some similarities with one derived for long-wave shear instability (Balmforth & Young 1997).
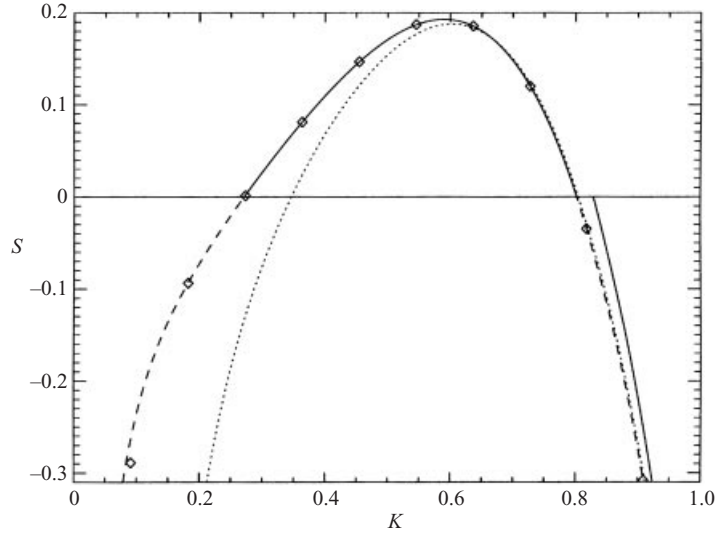
FIGURE 9. Growth rate, S, as a function of wavenumber, K, for $Ri_5 = 0.05$. The solid line is the non-diffusive case ($Pe = \infty$), the dashed line is the weakly diffusive case ($Pe \sim \epsilon^{-10}$), and the dotted line is computed using the asymptotic theory for $Pe = O(1)$. The diamonds are taken from numerical solutions to the amplitude equations (5.3)–(5.4) with a finite domain in Z.

5.1. *A dispersion relation*

On neglecting the nonlinear terms, we find that the normal modes, with dependence $\exp(iK\xi + S\tau)$, satisfy

$$iK \left[S + \frac{3}{\sqrt{2}}K^4 - \sqrt{2}K^2 \right] A = -\frac{Ri_5}{\pi} \int_{-\infty}^{\infty} \Theta \, dZ, \qquad (5.5)$$

$$(S + iKZ)\Theta - \mu\Theta_{ZZ} = iKA, \qquad (5.6)$$

and one can derive the dispersion relation,

$$S = \sqrt{2}K^2 - \frac{3}{\sqrt{2}}K^4 - \frac{\sigma}{|K|}Ri_5, \qquad (5.7)$$

where $\sigma = 1$ if $\mu \neq 0$, but $\sigma = \mathrm{sgn}(S)$ if $\mu = 0$, (cf. Balmforth & Young 1997). The two versions of the dispersion relation are drawn in figure 9, and neutral stability boundaries computed using this formula are presented earlier in figure 5.

The growth rate for finite Péclet number (the dashed line in figure 9) is a smooth function of wavenumber. However, the non-diffusive curve (the solid line) is discontinuous. This reflects the singular nature of the non-diffusive linear eigenvalue problem that was mentioned in §3; the lack of a common limit as $c_i \to 0$ from either above or below (or equivalently $S \to 0^{\pm}$) is seen clearly in the figure. The peculiar behaviour arises from the final, stabilizing, stratification term in (5.7). The presence of this dissipative term is, in fact, quite surprising for $\mu = 0$ ($Pe_{10} \to \infty$): in this limit, the temperature field is simply advected around without diffusive decay, yet this action still acts to damp the global mode. The reason is that the temperature field becomes increasingly filamentary as it is advected and twisted up by the mode, with the result that its integral moments decay with time. This leads to an apparent diffusive effect, and is closely related to the phenomenon of Landau damping in plasmas, in which

the distribution function (the analogy of Θ) becomes filamentary and its integral (related to the electric field) decays with time.

5.2. *Quasi-steady, single-mode boundary layers*

There are some limits of the amplitude equations that are amenable to further analysis. The first limit is obtained when $Ri_5 \ll 1$ and the horizontal domain size, $2\pi L$, is specially selected so that there is a single Fourier mode, $A_1 \sim \exp(\mathrm{i}\xi/L)$, with a low (positive) growth rate, and the remainder, $A_n \sim \exp(\mathrm{i}n\xi/L)$ with $n < 1$, are, comparatively, much more strongly damped. This sets the stage for a further reduction of the problem, namely a projection onto the special mode.

Let $\xi = L\xi'$, $T = \delta\tau$ and $Ri_5 = \pi\delta\Lambda/L$, where $\delta \ll 1$ denotes the growth rate of the weakly unstable mode. A Fourier decomposition of A then indicates that $A_n = O(\delta)$ for $n > 1$, and

$$A_{1T} - A_1 = \frac{\mathrm{i}}{2\pi}\Lambda \int_0^{2\pi} \mathrm{d}\xi \int_{-\infty}^{\infty} \mathrm{d}Z\, \mathrm{e}^{-\mathrm{i}\xi}\Theta(\xi, Z, T) \tag{5.8}$$

(after dropping the prime). Moreover, to order δ,

$$Z\Theta_\xi - \check{A}_\xi + \check{A}_\xi\Theta_Z = \mu L\Theta_{ZZ}, \tag{5.9}$$

where $\check{A}(\xi) = A_1\mathrm{e}^{\mathrm{i}\xi} + \mathrm{c.c.}$ Thus, the slow growth of the unstable mode permits the boundary layer to evolve into a quasi-steady state.

Now we borrow some analysis from Churilov & Shukhman (1996): define $A_1 = -a(T)\mathrm{e}^{\mathrm{i}\varphi}(T)$, $\Xi = \xi + \varphi$ and $\eta = Z/\sqrt{2a}$. Then,

$$\eta\Theta_\Xi + \Theta_\eta \sin\Xi - \lambda\Theta_{\eta\eta} = \sqrt{2a}\sin\Xi, \tag{5.10}$$

where $\lambda = \mu L/(2a)^{3/2}$, which is solved in terms of a special function, $g_1(\Xi, \eta, \lambda)$, constructed by Churilov & Shukhman:

$$\Theta = -\sqrt{\frac{a}{2}}\, g_1(\Xi, \eta; \lambda). \tag{5.11}$$

Thence,

$$a_T = a + \Lambda a\Phi_1[\mu L/(2a)^{3/2}], \quad \varphi_T = 0, \tag{5.12}$$

where $\Phi_1(\lambda)$ is another tabulated function which decreases monotonically from $\Phi_1(0) = 0$ to $\Phi_1 \to -\pi$ as $\lambda \to \infty$. For low amplitudes, $a_T \sim (1 - \pi\Lambda)a$, which is a re-expression of the linear result in (5.7). Also, provided $1 > \pi\Lambda$, a continues to increase with time, and eventually diverges more quickly: $a \sim \mathrm{e}^T$. Simultaneously, because $Z = \eta\sqrt{2a}$, the boundary layer thickens.

The divergence of a, and the expansion of the scale of the boundary layer, indicates that the effective diffusivity in (5.10) decreases with time. The relevant asymptotic solution for Θ is therefore one in which the total temperature field, $\eta + \Theta$, becomes swept around and averaged along the streamlines, $\Psi = \eta^2 + 2\cos\Xi = \text{constant}$. These streamlines are a slowly expanding set of curves much like the orbits of a pendulum, or the streamlines of the Kelvin cat's eye. Moreover, symmetry demands that $\eta + \Theta = 0$ within the separatrices. In other words, as the unstable mode grows, it twists up and homogenizes the temperature field inside cat's eyes that emerge within the boundary layers. Such mixed layers were in fact observed in experiments with electrolyte fluids (Batchayev *et al.* 1984).

5.3. *A single-wave model*

If the diffusivity μ is small in the situation described above, then the boundary layer cannot evolve into a quasi-steady state as the unstable mode grows. In this limit, we need another scheme for rescaling the amplitude equations:

$$\left. \begin{array}{lll} \xi \to L\xi', & Z \to L\delta\zeta, & A_1 \to L^2\delta^2 A_1', \\ \Theta \to L\delta\Theta', & Ri_5 \to \pi\delta^2\tilde{\Lambda}, & \mu \to L^2\delta^3\tilde{\lambda}. \end{array} \right\} \qquad (5.13)$$

Then, after removing the prime,

$$A_{1T} = A_1 + \frac{\mathrm{i}}{2\pi}\Lambda \int_0^{2\pi} \mathrm{d}\xi \int_{-\infty}^{\infty} d\zeta \mathrm{e}^{-\mathrm{i}\xi}\Theta(\xi,\zeta,T) \qquad (5.14)$$

and

$$\Theta_T + \zeta\Theta_\xi - \mathrm{i}(A_1\mathrm{e}^{\mathrm{i}\xi} - A_1^*\mathrm{e}^{-\mathrm{i}\xi})(1 - \Theta_\zeta) = \tilde{\lambda}\Theta_{\zeta\zeta}. \qquad (5.15)$$

This reduced system is similar to models derived for shear instability (Churilov & Shukhman 1987; Goldstein & Hultgren 1988) and in plasma physics (O'Neil, Winfrey & Malmberg 1971), with one essential difference: in the current theory, the global mode itself is unstable, and is damped by diffusion or Landau damping within the boundary layer; in the other models, the global mode itself is not directly unstable, and the instability arises from equilibrium gradients within the inner region (background vorticity gradients for the shear flows). Despite this difference, by analogy with those other problems, we anticipate that the global mode twists up the field Θ into a cat's eye structure, and any diffusion causes the cat's eye to spread. These expectations are confirmed by the numerical computations shown in figure 10.

The numerical solution also illustrates how the unstable mode fails to saturate as the temperature field twists up, but, in fact, begins to grow more rapidly. This parallels the quasi-steady version of the theory and reflects how the redistribution of the mean temperature field gradually flattens the average temperature gradient inside the boundary layer. Because the reduced gradient is less effective in impeding the instability, the growth of the mode then accelerates. Thus the mode gradually frees itself of the stabilizing effect of stratification and grows with a rate closer to the unstratified problem. This divergent behaviour is quite unlike the behaviour found for critical layers, but is a natural consequence of the competition between the viscous global instability and the stabilization provided by background gradients in the boundary layer. The situation has some similarities with reduced models of baroclinic instability (Warn & Gauthier 1989) and thermohaline convection in a slowly diffusing salt field (Balmforth & Casti 1998).

5.4. *Numerical solutions*

The previous two subsections outlined asymptotic limits in which we can make some connections with earlier theories for related problems and obtain images of cat's eye patterns of mixed regions within slowly expanding boundary layers. This phenomenology also extends to the full long-wave theory, which we solve numerically using a pseudospectral code and a finite computational domain in Z. The size of the computational box is sufficiently large to ensure roughly the same growth rates as the linear theory (see figure 9); the box size in the streamwise direction is 70 and in the cross-stream direction is 50. The code is initialized with a low-amplitude mode with eight horizontal wavelengths in the box, and figure 11 shows the ensuing evolution.

But for the array of cat's eyes, the evolution is much the same as before: as
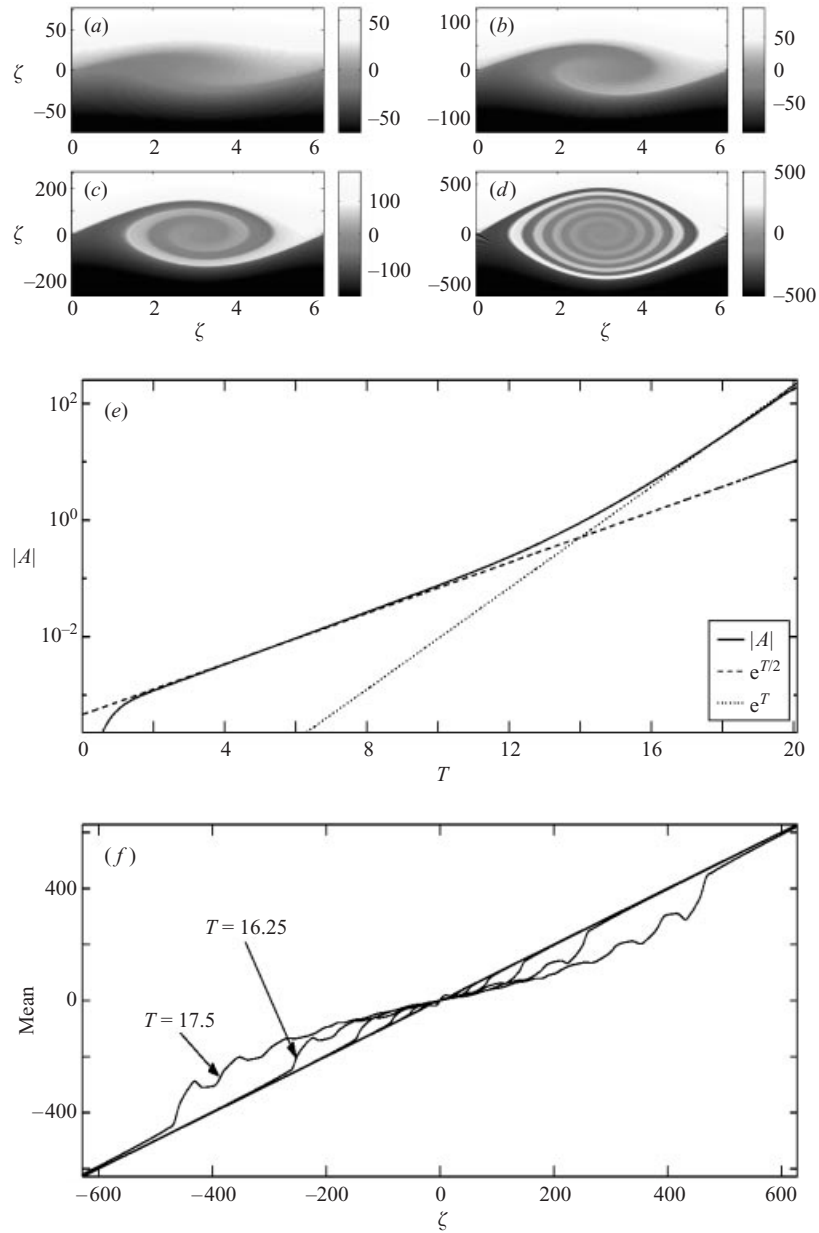
FIGURE 10. Simulation of the single-wave model (5.15) for $\tilde{\varLambda} = 1/(2\pi)$ and $\tilde{\lambda} = 10^{-6}$. (*a–d*) Snapshots of the total temperature field $\zeta + \Theta(\xi, \zeta, T)$: (*a*) $T = 10$, (*b*) $T = 12.5$, (*c*) $T = 15$, (*d*) $T = 17.5$. The colourmap used in each panel is different and is also displayed. (*e*) The corresponding evolution of $A_1(T)$, together with the trends of the actual linear instability ($\exp(T/2)$), and the instability without stratification ($\exp T$). Finally, (*f*) illustrates how the growing mode redistributes the mean temperature field inside the boundary layer, slowly flattening the mean gradient. The numerical scheme is similar to that used in Balmforth *et al.* (2001), with a domain in ζ of $[-400\pi, 400\pi]$, 1025 gridpoints in ζ and 256 in ξ.
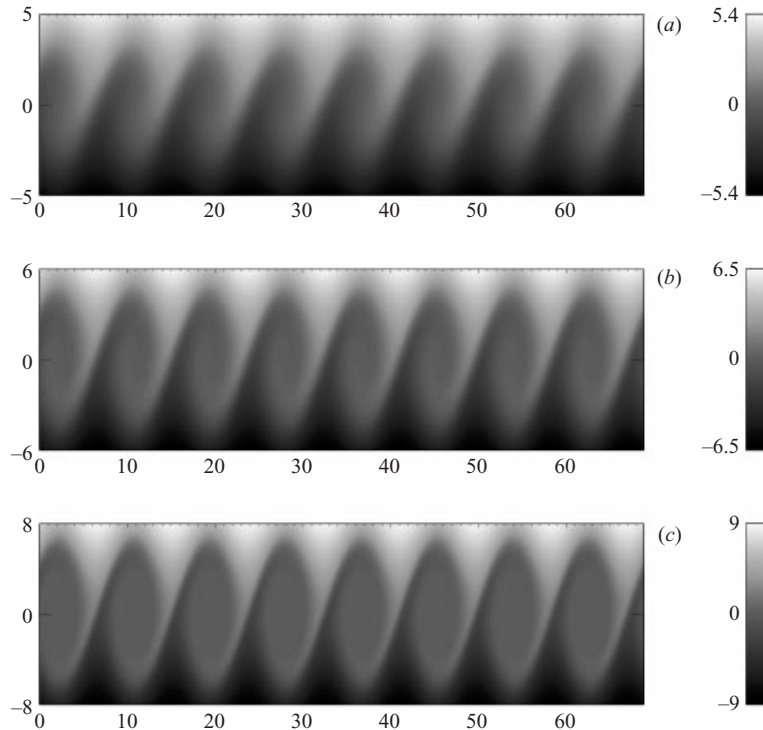
FIGURE 11. Snapshots of the total temperature at times, (*a*) $t = 20$, (*b*) 26, and (*c*) 32 for $Ri_5 = 0.05$ and $\mu = 1.0$ in equations (5.3) and (5.4).

time proceeds, the swirl around the centre of each cell demolishes the temperature gradients inside the cat's eyes and concentrates that gradient in thin stripes at the cell peripheries (the cat's eyelids). The destruction of the stratification serves, once again, to release the instability, which at later times grows faster. The acceleration of the modal growth is shown in figure 12.

We have also conducted simulations with different initial conditions and different values for the stratification parameter Ri_5. In all cases, one mode dominates during the linear growth phase leading to a cat's eye pattern with a given spatial periodicity. The subsequent evolution then follows a similar route to that shown in figure 11; the boundary layer inexorably expands.

The unabated expansion indicates that the boundary layer theory does not capture the saturation and long-time dynamics of the instability, unlike the long-wave equation of §4. That is, the large Péclet number theory captures only an initial transient. This transient ends when the scale of the boundary layers becomes comparable to the size of the original system. At this juncture, the boundary layers experience the variation of the sinusoidal basic flow and interact with one another. Unfortunately, we cannot explore this stage of the dynamics analytically and we turn to numerical simulations to resolve the fate of the inverse cascade.

6. Direct numerical simulation

In this section we present results from numerically simulating the full system (2.1)–(2.2) with a parallel pseudospectral code. (The code is fully parallelized in MPI, and
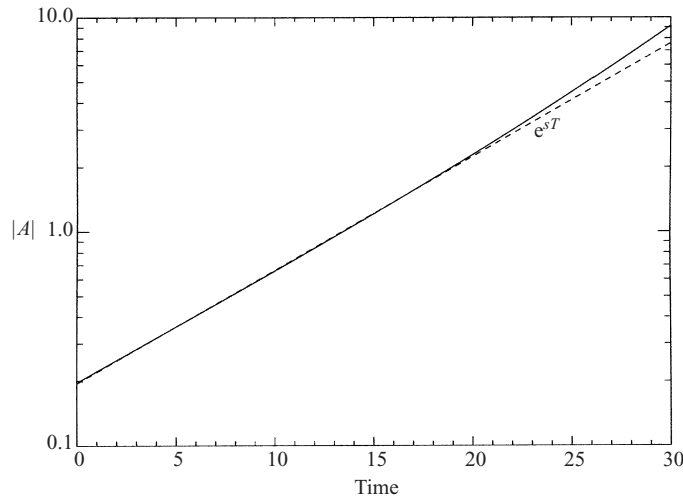
FIGURE 12. Integral average of A as a function of time (solid line). The dashed line shows the linear growth rate.

has been tested for both spatial and temporal convergences on SGI Origin.) The numerical resolution, if not mentioned otherwise, is 512×512, and was sufficient to resolve the smallest scales that developed in the simulations. The code assumes periodic boundary conditions in both directions, and the runs begin with random fields of very small amplitude. The aspect ratio of the computational box is first fixed at 8 (streamwise to cross-stream) so that there is one wavelength of the basic sinusoidal flow in the vertical, but eight wavelengths would fit in the horizontal. For these flows, we vary the Péclet number and Reynolds number, and fix the stratification strength, $Ri = 0.01$. Later, we consider flows with aspect ratios of unity, fix Re, and vary Ri and Pe.

There are three main goals in this section. First, the asymptotic theories described above have limited ranges of validity. It is therefore of interest to advance beyond these limitations and explore the dynamics over a much wider parameter regime. Second, our analysis of the large Péclet number problem exposed a flaw in the relevant long-wave theory, namely that solutions always diverge as the boundary layer inexorably expands. To study what happens beyond this transient dynamics, we simulate the full equations with relatively high Péclet numbers. Finally, our chief aim in this article is to explore the effect of stratification on the inverse cascade found in the Kolmogorov problem. The asymptotic theories go some way to determine how stratification modifies the problem, but our numerical simulations progress much further in providing a broad understanding over a wider parameter range.

6.1. *Beyond onset*

We focus first on a low Péclet number case, $Pe = 1$; in the next section we explore what happens at higher Pe. As illustrated in figure 13, for Reynolds numbers as large as 40, the system evolves to a stationary state; this figure shows the amplitude of the instability, as measured by the average speed of the disturbance to the basic shear flow $(\sqrt{\langle \psi_x^2 + \psi_z^2 \rangle}$, where the angular brackets denote the integral average over the domain). In the final state, the solution takes the form of a sequence of meandering jets, with vortices occurring within part of the meander; the stratification is modified according to the advection by this flow (see figure 14).
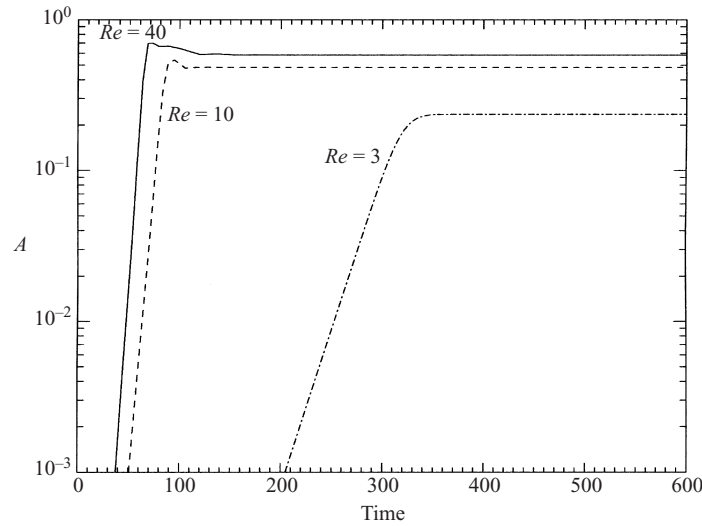
FIGURE 13. Amplitude (defined as the integral average of the speed associated with the disturbance) for different Reynolds numbers with $Pe = 1$ and $Ri = 0.01$.
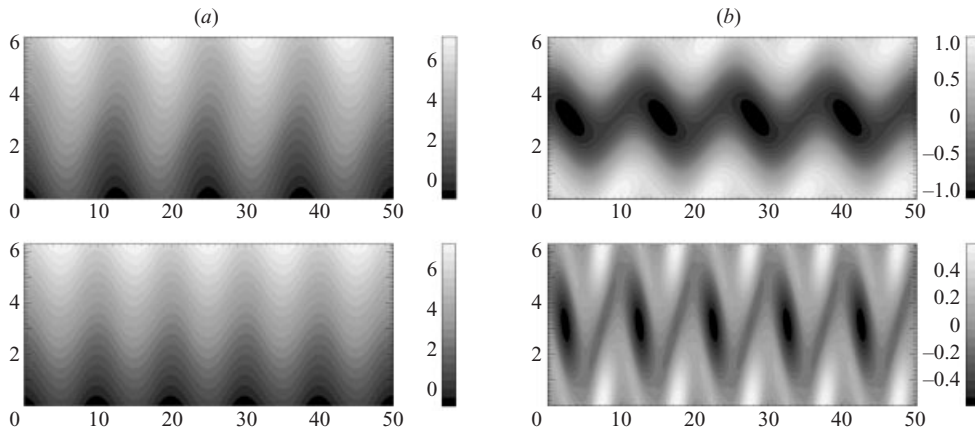

FIGURE 14. Final, stationary solutions for $Pe = 1$: (*a*) total temperature, and (*b*) total vorticity for $Re = 3$ (upper panels) and 40 (lower panels).

At $Re = 3$ there are four meanders in the box and there is no sign of a coarsening of the pattern. At higher Reynolds number, the meandering has larger amplitude and the vortices within the meanders are intensified. However, the overall pattern remains the same except that five meanders now occur. Stratification therefore arrests the inverse cascade, in agreement with the asymptotic analysis, but the simulations show how the arrest of the inverse cascade continues to much higher Reynolds numbers. The change in the pattern wavelength is also consistent with the results of §4, where we found multiple equilibria with varying wavelength. However, we have not varied the initial condition to verify the existence of multiple final states in the full simulations.

6.2. *Expanding boundary layers*

At larger Péclet numbers, the numerical simulations confirm the generation of thermal boundary layers containing cat's eye patterns, see figure 15. The layers expand
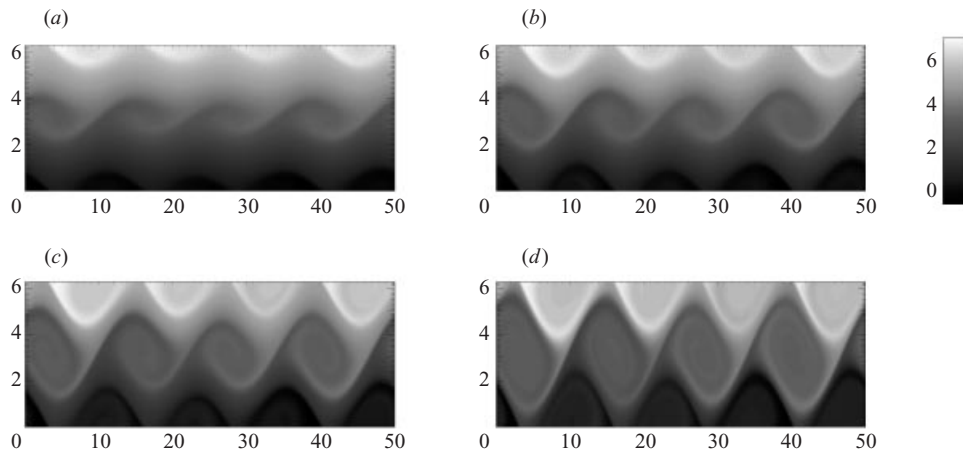
FIGURE 15. Evolution of the internal boundary layer for $Pe = 400$, $Re = 3$ and $Ri = 0.01$. The times of the snapshots are (*a*) $t = 222$, (*b*) 234, (*c*) 247 and (*d*) 211. We observe similar evolution for $Pe = 100$.
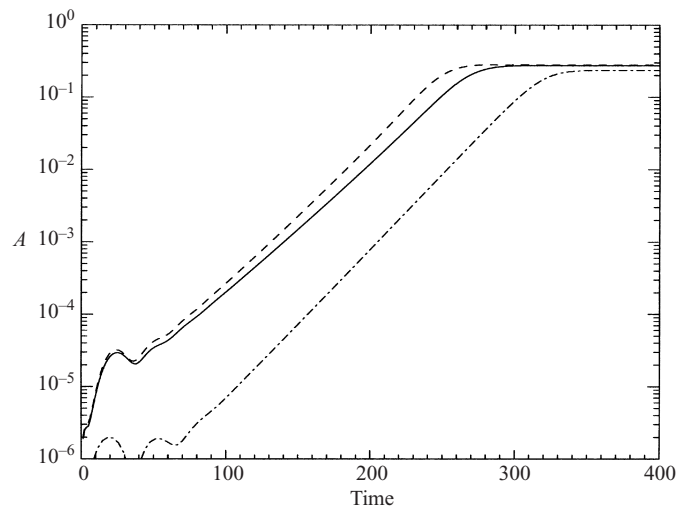

FIGURE 16. Amplitude (defined as the integral average of the speed associated with the disturbance) for different Péclet numbers with $Re = 3$ and $Ri = 0.01$. The dashed line is for $Pe = 400$, the solid line is for $Pe = 100$, and the dash-dotted line is for $Pe = 1$.

(approximately exponential in time, in line with results of §5), reaching the scale of the basic shear flow whereupon they interact with one another. The layers adjust to one another's shape and approach a 'checkerboard' pattern of well-mixed vortices separated by diffusive interfaces. For $Re = 3$, the checkerboard patterns are steady (figure 16); figure 17 compares the final states for $Pe = 100$ and 400.

At higher Reynolds number, the expanding boundary layers do not approach a steady state when they come into contact. Figure 18 shows the temporal behaviour of the amplitude for the two higher Péclet numbers. At $Re = 10$, the solution for $Pe = 100$ is periodic, and that for $Pe = 400$ is aperiodic, and possibly chaotic. When we raise the Reynolds number further to 40, both $Pe = 100$ and $Pe = 400$ solutions appear chaotic. However, we have not systematically traced the transition from the
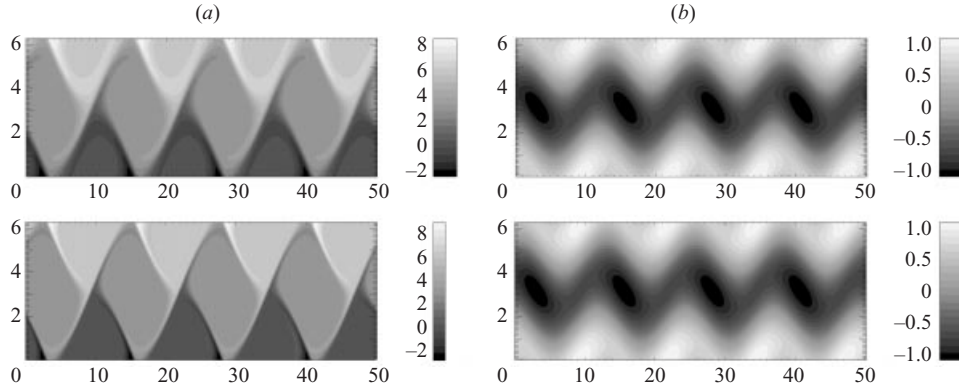
FIGURE 17. Final snapshots of temperature (*a*) and total vorticity (*b*). The Péclet number is
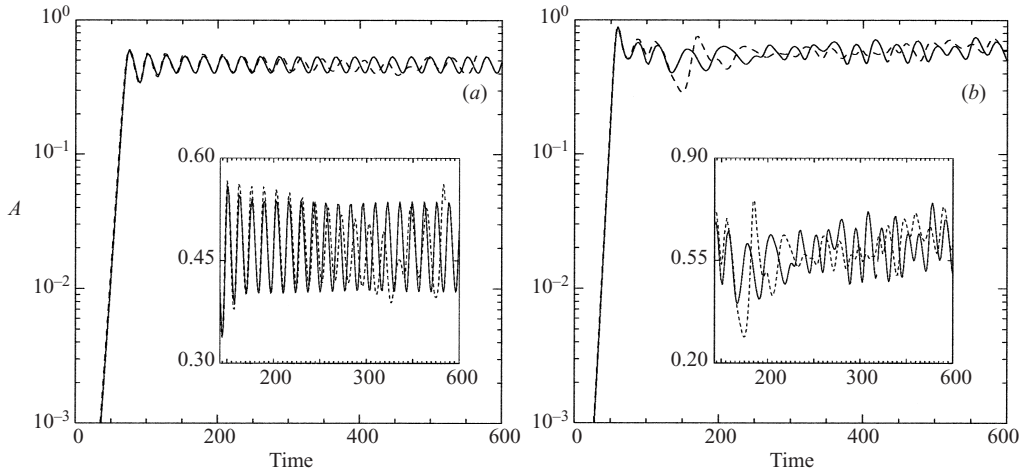100 (top) and 400 (bottom).

FIGURE 18. Amplitude (the integral average of the speed associated with the disturbance) for
different Péclet numbers with $Re = 10$ (*a*), $Re = 40$ (*b*) and $Ri = 0.01$: the dashed line is for
$Pe = 400$ and the solid line is for $Pe = 100$.

steady equilibria at lower Reynolds number to these unsteady states, and so we
cannot say what bifurcations have led to the apparent chaos. Moreover, there may
again be multiple states, some of which could be steady. Our chief aim here is not
give to a bifurcation study like that undertaken in Platt *et al.* (1991), but to convey
some idea of the flavour of the dynamics that arises at higher Reynolds number for
different Péclet numbers. (It is not clear how useful such a study would be, given
that a multitude of bifurcations probably occur – we might simply become lost in the
maze of the bifurcation sequence.)

The oscillations for $Re = 10$ and $Pe = 100$ reflect pulsations of the meander
of the jets in combination with nutations of the vortices; we show snapshots of the
temperature and vorticity fields at times during one cycle in figure 19. Because thermal
diffusion is now relatively slow, the pulsation significantly rearranges the temperature
field, and generates a periodic exchange of kinetic and potential energy between the
meandering jets and the embedded vortices. In fact, the oscillation period (about 30
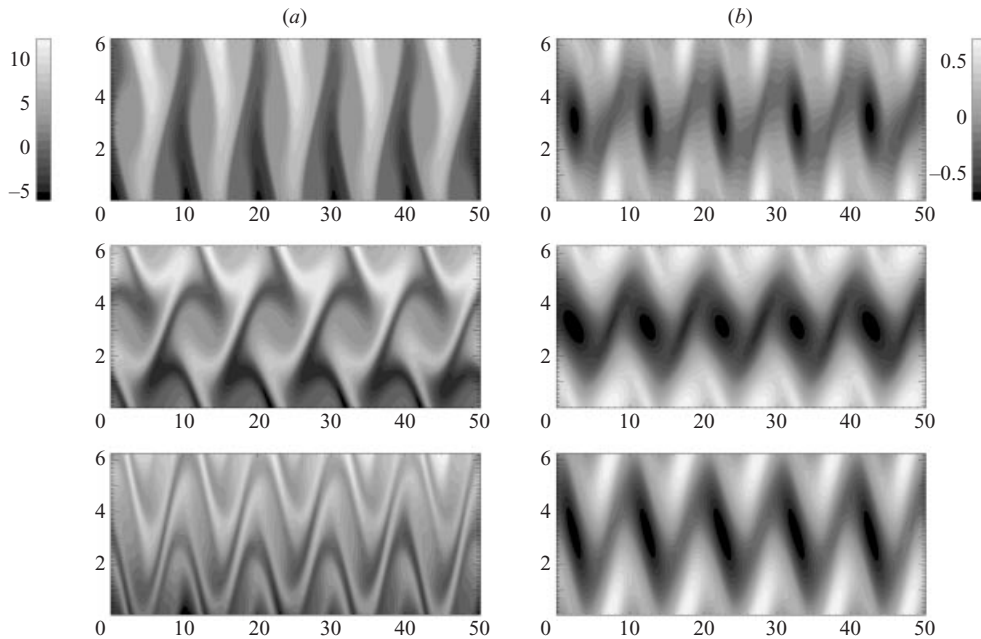time units), is not very different from $2\pi/\sqrt{Ri} \approx 60$, the lower bound on the gravity

FIGURE 19. Pulsating meander for $Re = 10$, $Pe = 100$, and $Ri = 0.01$: (*a*) snap-shots of total temperature and (*b*) the total vorticity. The times of the snapshots are $t = 82$, 90 and 98 (top to bottom). A movie of the entire simulation corresponding to this figure is available at http://astro. uchicago.edu/home/web/young/linkdir/SKS001.html.

wave periods in the absence of the Kolmogorov flow. Moreover, because temperature gradients are amplified by the fluid motions (see below), the gravity wave periods are smaller in the evolving Kolmogorov flow. Hence, we interpret the cycling as resulting, at least in part, from the influence of buoyancy. The cycling does not occur at lower Péclet number because thermal diffusion rapidly obliterates the temperature variations that provide the buoyancy forces.

The amplitude pulsation of the meander and the nutation of the vortices is also evident at $Re = 10$ and $Pe = 400$. However, the oscillation does not remain regular in this case, and vortices begin drifting horizontally (see figure 20). This motion permits strong interactions to occur amongst the vortices that result in mergers. In this way, the total number of vortices decreases, leading to an overall lengthening of the characteristic spatial scale. This unsteady redistribution of vortices is somewhat like that in numerical experiments on two-dimensional turbulence (McWilliams 1990), and shallow-water flows of Jupiter's winds (Williams & Wilson 1988) and on the surface of a sphere (Cho & Polvani 1996). However, vortex mergers do not continue to occur, and there is no subsequent inverse cascade. Instead the jets suffer further instabilities that produce more vortices. This furnishes a state with intermediate characteristic lengthscales in which the vortices and jets are in a chaotic balance or 'weakly turbulent equilibrium'.

At higher Reynolds number $Re = 40$, there is a somewhat similar picture for the evolution and we illustrate this with $Pe = 400$ (figure 21). As before, evolution commences when thermal boundary layers form and the jets begin to meander. However, the expanding cat's eyes grow so quickly that they mix the temperature field everywhere except in the sharp interfaces corresponding to the cat's eyelids.
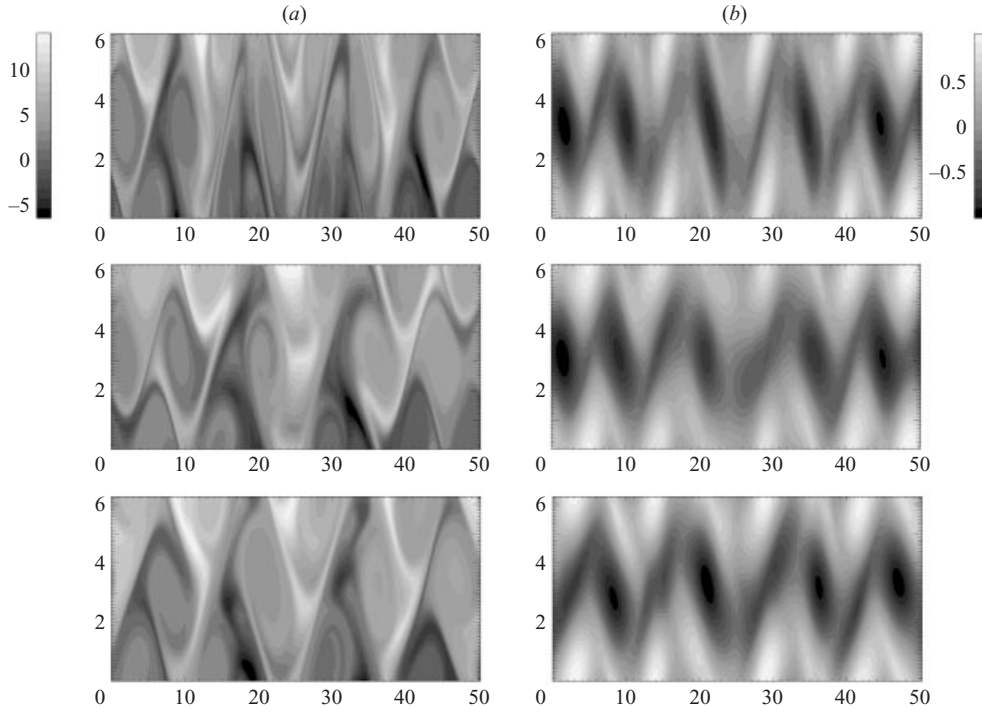
FIGURE 20. Unsteady vortices and mergers for $Re = 10$, $Pe = 400$, and $Ri = 0.01$: (a) panels are snap-shots of total temperature and (b) the total vorticity. The times of the snapshots are $t = 380$, 450 and 507 (top to bottom). A movie of the entire simulation corresponding to this figure is available at http://astro.uchicago.edu/home/web/young/linkdir/SKS002.html.

These interfaces grow with the meander of the jet, traversing about three vertical periods of the basic flow, and never truly come into contact with their counterparts above and below. No checkerboard pattern forms from this evolution. Instead, the meander breaks down and the original horizontal jets take over, tilting over the remnants of the highly elongated boundary layers and effectively mixing the fluid. From the resulting incoherent state, the linear instability begins a second phase of growth. The top three panels of figure 21 cover this period of the evolution. The second phase of the linear instability is interrupted by a different kind of dynamics that persists for the remainder of the computation: at about $t = 230$, the meander loses its spatial periodicity, and the jets break up into a number of interacting vortices. Subsequently, the jet-like sturctures reappear as vortices merge together. These motions lead to irregular pulsations of the horizontal flow (figure 22 – note how the instability significantly weakens the background horizontal flow, and so the vorticity imparted by the forcing becomes concentrated into the smaller-scale vortices), and produce the aperiodic cycles in the amplitude measure of figure 18. Overall, the evolution is similar for both $Pe = 100$ and 400, and is like a more erratic version of that occurring at lower Reynolds numbers. However, superposed on the pulsating meander is a large-scale 'sloshing' motion that is very reminiscent of a gravity wave. Roughly two wavelengths of the sloshing motion occur inside the domain. The bottom four panels of figure 21 show snapshots of the wavy, pulsating jets and vortices.

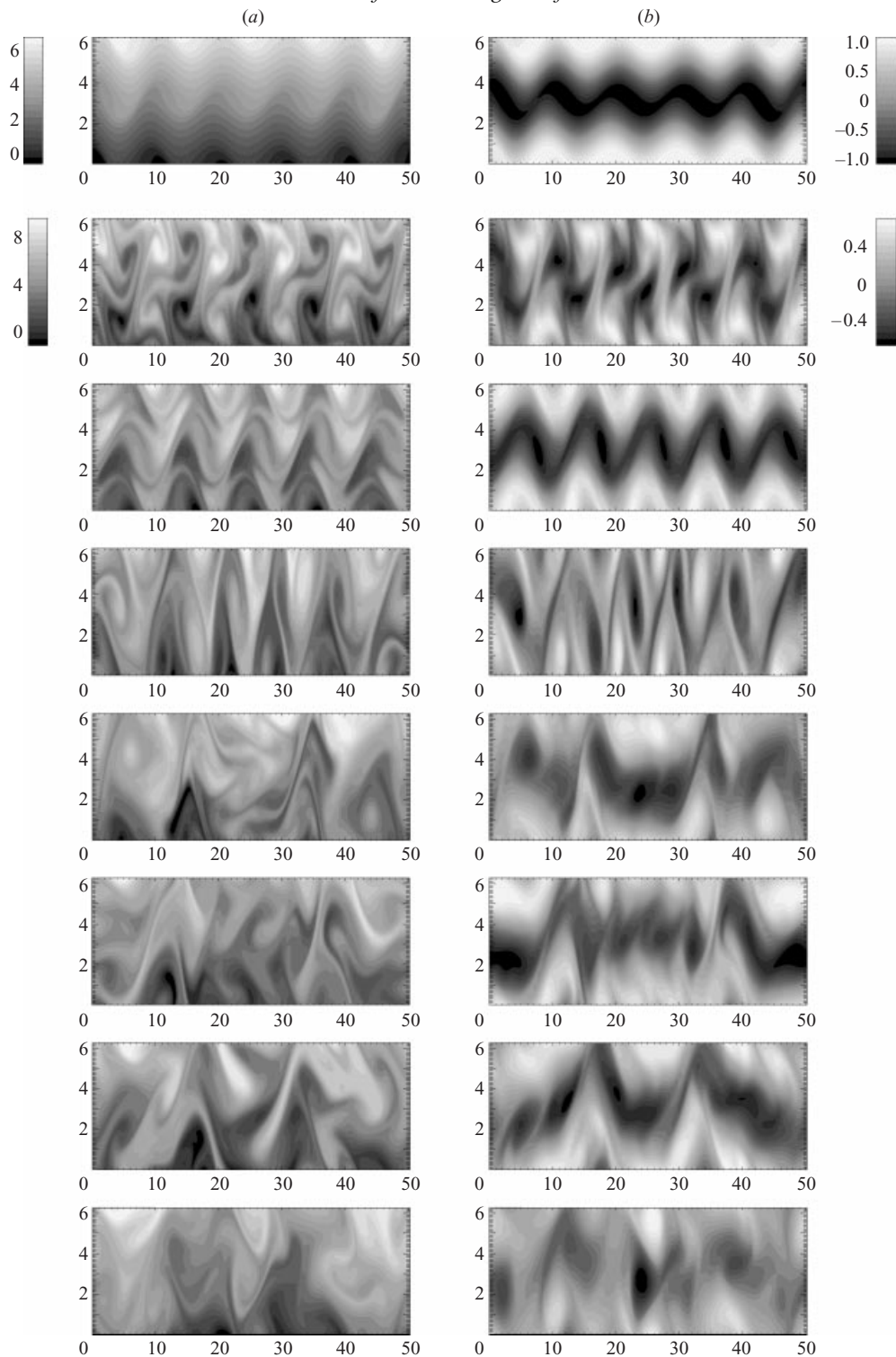   To try to quantify the character of the flow further, we compute a variety of global

FIGURE 21. Evolution at $Re = 40$ and $Pe = 400$: (a) snap-shots of total temperature and (b) total vorticity at $t = 49, 103, 158, 235, 267, 375, 485$ and 624 (top to bottom). As indicated by the keys, the colormap is the same for all snapshots but the first. A movie of the entire simulation corresponding to this figure is available at http://astro.uchicago.edu/home/web/young/linkdir/SKS003.html.
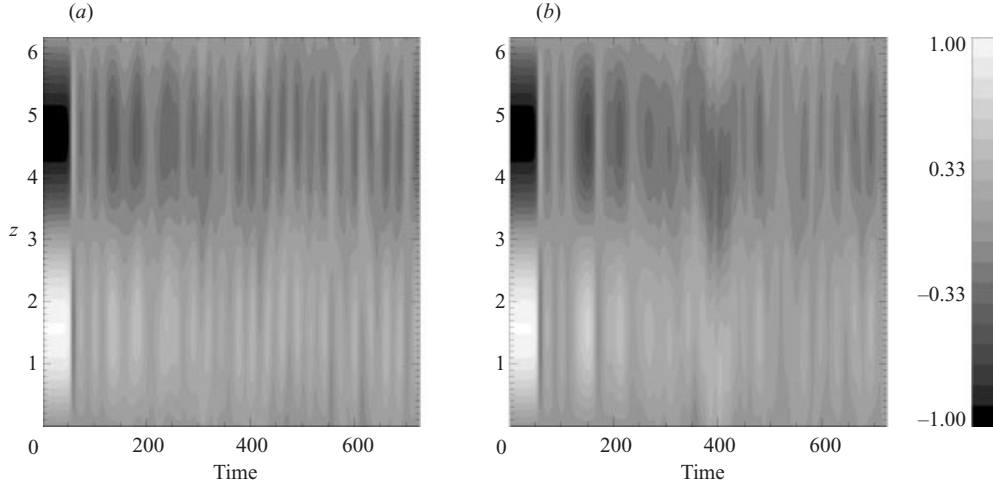
FIGURE 22. Evolution of the horizontally averaged, horizontal flow for $Re = 40$ and $Ri = 0.01$:
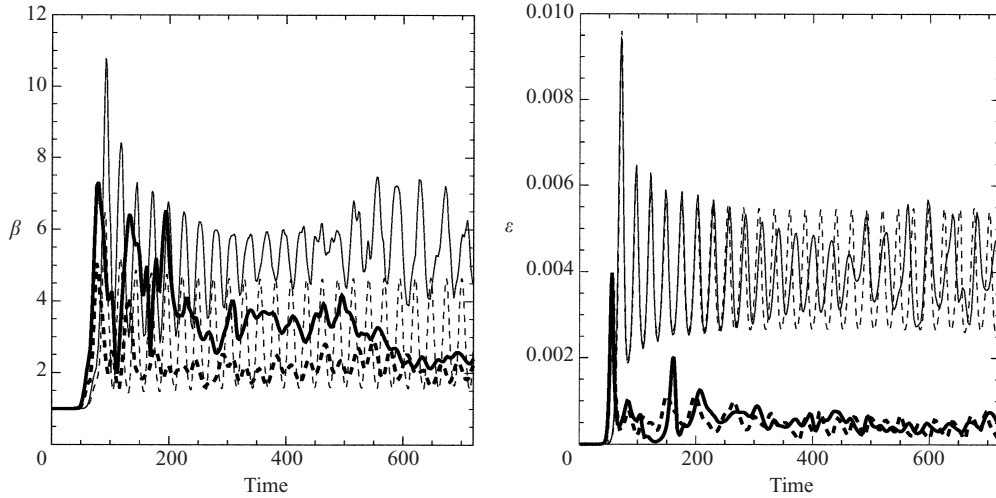(*a*) $Pe = 100$, (*b*) $Pe = 400$.

FIGURE 23. Evolution of β and ε for $Pe = 100$ (dashed lines) and $Pe = 400$ (solid lines).
The thick lines are for $Re = 40$ and the thin lines are for $Re = 10$.

measures of the dynamics. First, we estimate the average (dimensionless) vertical temperature gradient and energy dissipation measure associated with the 'eddies',

$$\beta = \langle T_z \rangle, \quad \varepsilon = \frac{1}{Re}\langle 4\tilde{u}_x^2 + (\tilde{u}_z + w_x)^2 \rangle, \tag{6.1}$$

where the angular brackets denote the volume average, and the tilde indicates the departure from the horizontal average. Figure 23 shows the temporal evolution of the two quantities for $Re = 10$ and 40, and for both $Pe = 100$ and 400. Evidently, the instability significantly sharpens the effective temperature gradient. The rapid variations before $t \sim 200$ in both β and ε are caused by the rapid broadening of the internal layers and their subsequent destruction during the pulsating meandering state. Vortex mergers near $t = 500$ are also signified by more gradual decreases in β for $Re = 40$.

Lengthscale	Definition	$Pe = 100$	$Pe = 400$
l_u	$2\pi\sqrt{\langle u^2\rangle/\langle u_x^2\rangle}$	22.1	20.5
l_ω	$2\pi\sqrt{\langle\omega^2\rangle/\langle\omega_x^2\rangle}$	13.4	10.5
l_b	$2\pi\sqrt{\langle w^2\rangle}\beta^{-1/2}Ri^{-1/2}$	7.5	6.3
l_O (Ozmidov)	$2\pi\varepsilon^{1/2}\beta^{-3/4}Re^{-1/2}Ri^{-3/4}$	0.4	0.3
l_K (Kolmogorov)	$2\pi\varepsilon^{-1/4}Re^{-1/2}$	6.9	6.7
l_B (Batchelor)	$2\pi\varepsilon^{-1/4}Pe^{-1/2}$	4.4	2.1
N (Buoyancy frequency)	$\beta^{1/2}Ri^{1/2}$	0.17	0.15

TABLE 1. Lengthscales for $Re = 40$ and $Ri = 0.01$. For each lengthscale, the definition and values for $Pe = 100$ and 400 are given. (The 2π appears because, in dimensionless units, that is the lengthscale of the Kolmogorov flow.) Also listed is the average buoyancy frequency. ($\varepsilon = 0.00041$ and 0.00048, and $\beta = 2.19$ and 2.87.) The resolution of the numerical scheme is about 0.1 in the horizontal, 0.01 in the vertical.

The measures, β and ε, are central quantities in estimating a variety of characteristic lengthscales in the theory of stratified turbulence (Smyth & Moum 2000). Though the physical conditions we are studying are far from turbulent, we also follow this direction to examine which lengthscales may characterize our simulations. We compute the lengthscales listed in table 1 (the values of β and ε used in table are temporal averages after $t \sim 200$). The first two lengthscales, l_u and l_ω, are integral measures of the characteristic horizontal scale of the horizontal velocity and vorticity, and are defined in analogy with the Taylor scale of turbulence theory. l_u appears to provide a crude measure of the characteristic horizontal lengthscales, and perhaps estimates the scale at which the inverse cascade is arrested and energy builds up. The vorticity scale l_ω roughly characterizes the size of the vortices that appear from the break-up of the jets. The buoyancy scale l_b estimates the maximal height that fluid parcels could rise given the average kinetic energy in the vertical flow component, and indicates that the flow is relatively energetic compared to the restoring force of gravity. In principle, fluid elements can rise through several vertical periods before decelerating to rest; such ascents were observed during the simulations. The Ozmidov scale, l_O, is commonly used to estimate of the lengthscale beyond which turbulent eddies experience a significant effect of stratification (Smyth & Moum 2000). Here, this lengthscale seems less useful and does not characterize the arrest of the inverse cascade. This is also why ε is so insensitive to Pe in figure 23.

6.3. *Inverse cascade over many scale heights*

Until now, we have considered a single vertical wavelength, or 'scale height', of the basic shear flow, in order to keep the problem simple and study the instability of a single vertical mode. With more wavelengths in the vertical, we admit more unstable vertical modes and the problem is enriched further (Friedlander & Howard 1998). We now extend our exploration by expanding the vertical domain, so that we may elaborate further on the arrest of the inverse cascade by considering much deeper flows for which stratification may have a more significant effect. Specifically, we choose the configuration used by She in his study of unstratified Kolmogorov flow (She 1987), with $Re = 22$, and consider varying strengths of stratification and Péclet number. The computational box has unit aspect ratio and a size of $16\pi \times 16\pi$, so there are 8 spatial periods of the sinusoidal flow. The initial conditions are random, low-amplitude superpositions of modes of wavenumbers between 20 and 40.
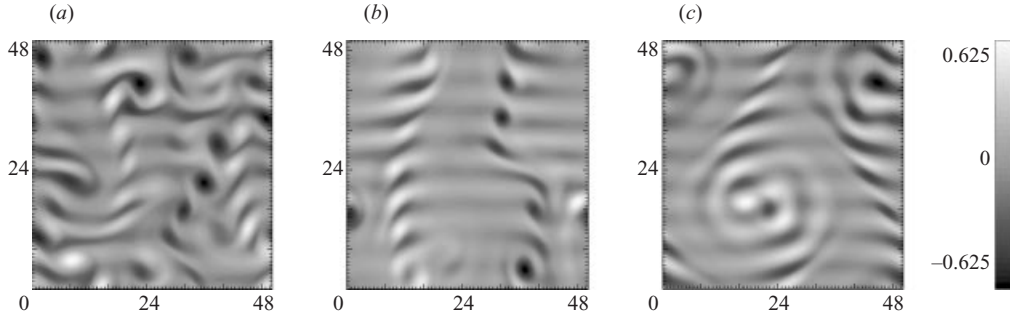
FIGURE 24. Inverse cascade in the unstratified case as large vortices form. $Re = 22$ and $Ri = 0$, and there are eight spatial periods in the background shear flow. The panels correspond to snapshots at times (a) 2600, (b) 3030 and (c) 3390. A movie of the entire simulation corresponding to this figure is available at http://astro.uchicago.edu/home/web/young/linkdir/SHE001.html.
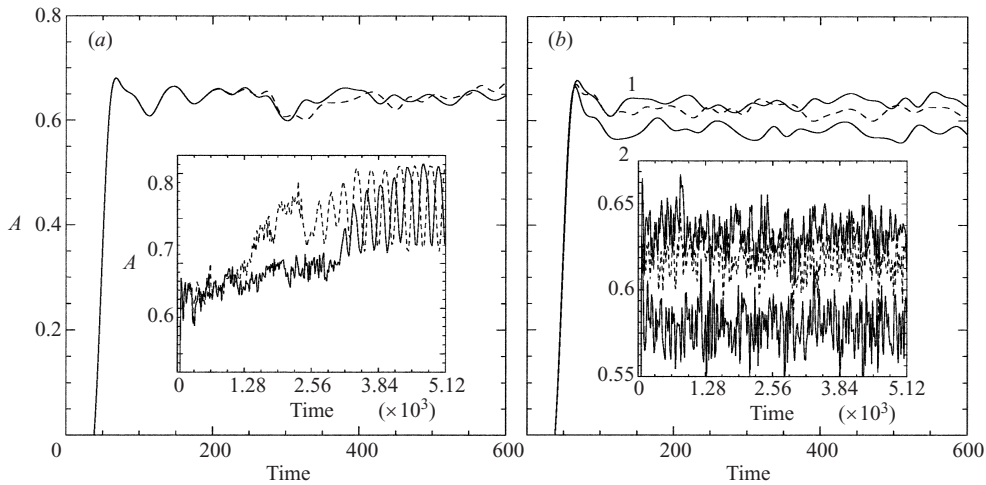

FIGURE 25. Average speed of the disturbance for (a) $Ri = 0$ (solid line) and 2.4×10^{-6} (dashed line) with $Pe = 1$, and (b) $Ri = 2.4 \times 10^{-4}$ (curve 1) 2.4×10^{-3} (curve 2) with $Pe = 1$. In (b), the dashed line shows $Ri = 2.4 \times 10^{-4}$ with $Pe = 40$.

For comparison with She's results, figure 24 shows snapshots of the unstratified inverse cascade. Figure 24(a) shows the unsteady state that is reached after the unstable modes saturate at relatively low amplitude (see figure 25a). After this initial saturation, the inverse cascade slowly builds up the disturbance until large-amplitude, long-period oscillations eventually set in. These oscillations arise due to the formation and rotation of two large vortical structures (figure 24c), which are similar to the dipole observed by She. The organization into large-scale fluid motion is also clearly revealed in the horizontal average of the horizontal velocity (figure 26).

Despite the formation of a dipole similar to She's computations, we were not able to observe any bursts. We may have failed to observe bursts because we did not continue the integrations to any great length, the arrest of the inverse cascade being our main focus. However, with $Re = 22$ and in runs of a similar length, we do observe bursts if we reduce the resolution to 256×256, the same spatial resolution as in She (1987). This suggests that bursts depend sensitively on resolution and may be numerical artifacts for $Re = 22$.
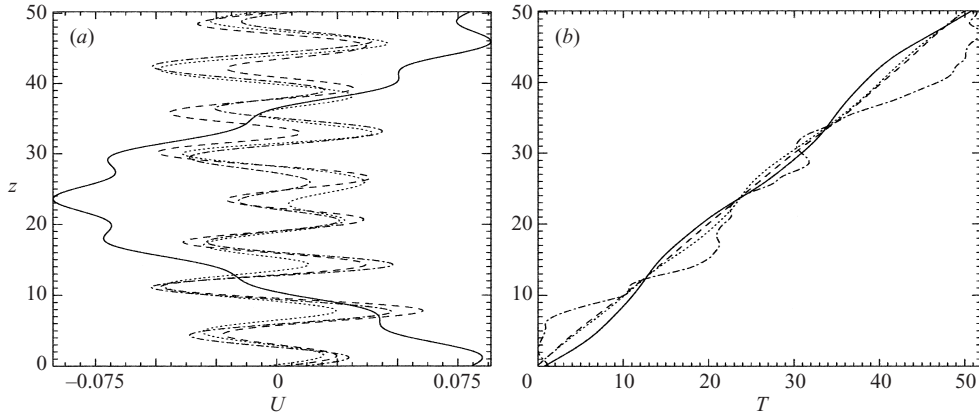
FIGURE 26. The final, horizontal average of (*a*) horizontal velocity and (*b*) temperature. The four cases shown are $(Re, Ri, Pe) = (22, 0, 1)$ (solid lines), $(Re, Ri, Pe) = (22, 0.016, 1)$ (dotted lines), $(Re, Ri, Pe) = (22, 0.16, 1)$ (dashed lines) and $(Re, Ri, Pe) = (22, 0.016, 30)$ (dashed and dotted lines).
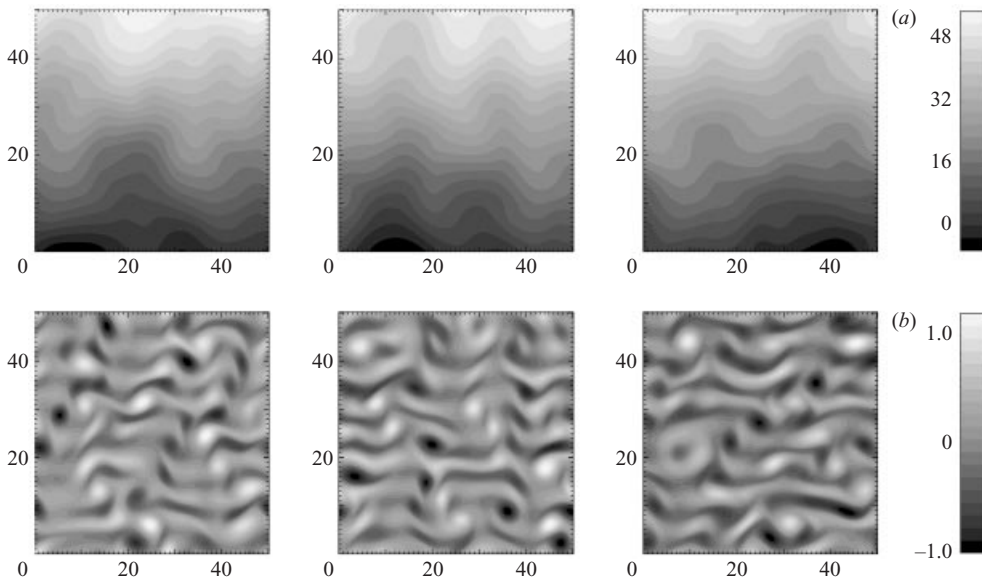

FIGURE 27. Total temperature (*a*) and total vorticity (*b*) for $Ri = 2.4 \times 10^{-4}$, $Re = 22$ and $Pe = 1$ at times 7770, 10298 and 12870. A movie of the entire simulation corresponding to this figure is available at http://astro.uchicago.edu/home/web/young/linkdir/SHE002.html.

Next, we add the temperature gradient, and first consider relatively small Péclet number, $Pe = 1$. For $Ri = 2.4 \times 10^{-6}$ we find flow patterns that are indistinguishable from the unstratified case and the inverse cascade seems largely unaffected. However, as we increase the Richardson number to 2.4×10^{-4} or 2.4×10^{-3}, the flow patterns change substantially (figures 27 and 28). Here, small-scale vortical structures form that are sharply confined in altitude; there seems little sign of an inverse cascade beyond the scale of these structures. The overall phenomenology is more similar to the unsteady meandering jets and vortices found earlier for flows with higher aspect ratio – roughly speaking, if we slice up the domain into sections of smaller aspect ratio, we recover pictures much like the figures of the previous subsection.
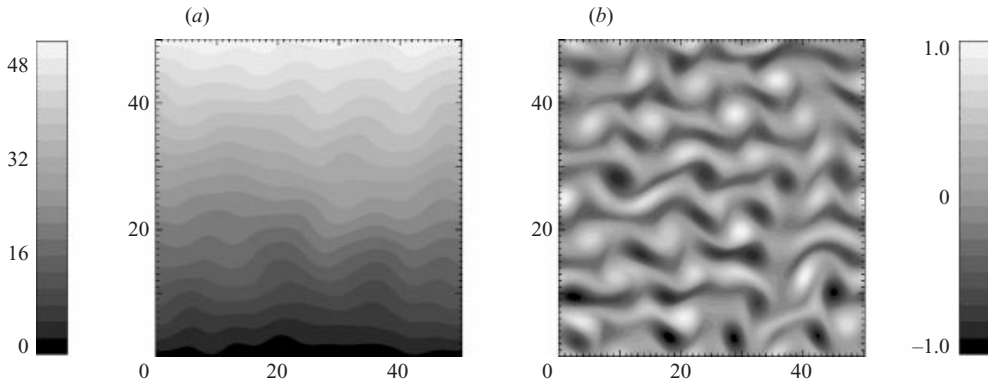
FIGURE 28. Total temperature (*a*) and total vorticity (*b*) for $Ri = 2.4 \times 10^{-3}$, $Re = 22$ and $Pe = 1$ at time 10611. A movie of the entire simulation corresponding to this figure is available at http://astro.uchicago.edu/home/web/young/linkdir/SHE003.html.

Stratification therefore inhibits the cascade of energy to large scales in both the horizontal and vertical. This inhibition is further illustrated in figure 29, where we show energy spectra. In particular, panels (*a*) and (*b*) show the evolving spectra for $Ri = 10^{-6}$ and $Ri = 2.4 \times 10^{-3}$, respectively. With $Ri = 10^{-6}$ (or $Ri = 0$), energy builds up quickly at small wavenumber, but for $Ri = 2.4 \times 10^{-3}$ there is little cascade. (The peaks at $k = 1$ reflect the energy input of the basic flow.)

The flow also has some effect on the stratification, but the temperature field remains relatively smooth in appearance and shows little trace of smaller-scale vortical structures. Indeed, the horizontal average of the temperature distribution remains close to the linear background (see figure 26). This is the signature of the strong thermal diffusion.

From the pictures of the vorticity or temperature distribution, one gains the overall impression of about two or three characteristic horizontal scales in the box for $Ri = 2.4 \times 10^{-4}$, and four or five for $Ri = 2.4 \times 10^{-3}$. These scales are also apparent in the relatively broad peaks around wavenumbers of 3/8–1/2 in the energy spectra of figure 29. However, the characteristic vertical scales are smaller and dominated by the energy-injection scale of the basic flow (eight wavelengths).

We compute characteristic lengthscales to try to quantify these observations further, see table 2. The velocity scale, l_u, roughly corresponds to the horizontal lengthscale, and the vorticity scale again estimates the size of small-scale vortices. The buoyancy scale once more identifies the flow as relatively energetic, and the Osmidov length predicts that stratification is only important to turbulent eddies with scales of the forcing or larger (because Ri is so much lower), but is otherwise unhelpful. Note that the forcing scale is below the dissipation scale (the Kolmogorov scale l_K) in the simulations, implying that the flow characteristics do not conform to the usual vision of turbulence in which the dissipation scales are the smallest in the system (and is why the spectrum shows none of the characteristic scalings of turbulence theory).

We conclude this section by raising the Péclet number to 40. In high aspect ratio domains, a change in the Péclet number significantly alters the patterns in temperature and even the dynamics. For unit aspect ratio, the dynamics appears to be mildly affected by a variation in the Péclet number, as shown by a slight change in the time series of the perturbation amplitude in figure 25(*b*). However, the time series are roughly equally erratic and it is difficult to conclude much from this global
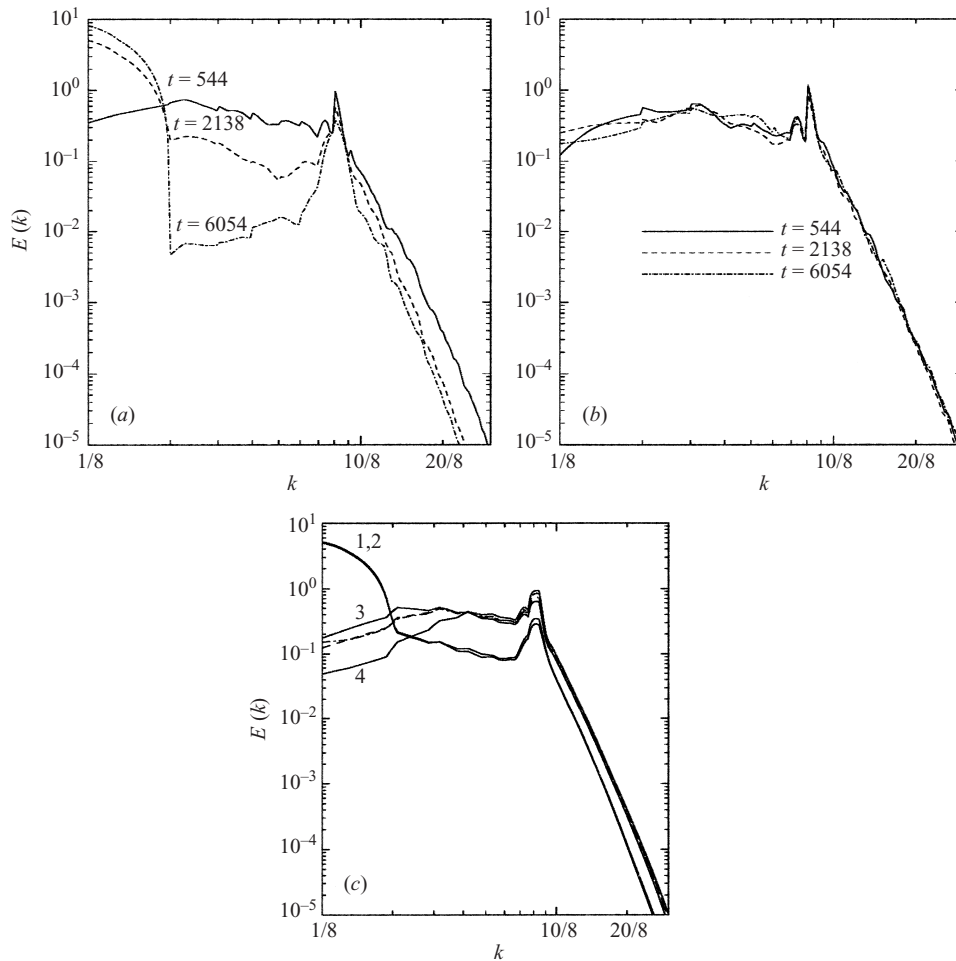
FIGURE 29. Three snapshots of the energy spectrum for (*a*) $Ri = 10^{-6}$ and (*b*) $Ri = 2.4 \times 10^{-3}$. (*c*) The final energy spectra for five computations: solid curves show spectra for $Pe = 1$ and (1) $Ri = 0$, (2) $Ri = 10^{-6}$, (3) $Ri = 2.4 \times 10^{-3}$ and (4) $Ri = 2.4 \times 10^{-2}$; the dashed line shows a case with $Ri = 2.4 \times 10^{-3}$ and $Pe = 40$.

measure. We gain more insight from figure 30 which shows snapshots of the vorticity and temperature fields. The temperature field now shows more structure, and there are clear signs of local temperature inversions. In fact, there are also reversals in the mean (horizontally averaged) temperature gradient (figure 26) similar to those seen in experimental data (Keller & Van Atta 2000), and suggests that static instability occurs at higher Péclet numbers.

In the horizontally averaged temperature field, there is some suggestion of 'layering' – the formation of well-mixed layers separated by sharp interfaces. Such features have been observed in stratified turbulent fluids in the laboratory (Park, Whitehead & Gnanadeskian 1994), in the ocean and in geological fluids (Turner 1985). Here, however, the evidence for layering is weak at best. Moreover, an examination of the unaveraged field (figure 30) shows little corresponding evidence. Instead, as brought out in figure 31, there are sharp, curved, thermal boundary layers with random inclinations in which most of the temperature variation is confined within a rela-

(Ri, Pe)	$(0, 1)$	$(2.4 \times 10^{-4}, 1)$	$(2.4 \times 10^{-3}, 1)$	$(2.4 \times 10^{-4}, 30)$
l_u	41.7	21.1	19.6	20.6
l_ω	11.6	11.6	11.6	11.6
l_b	∞	113.6	33.2	61.3
l_O	∞	23.6	4.6	10.1
l_K	9.0	7.0	6.8	6.9
l_B	43.1	33.2	32.2	6.0
N	0	0.016	0.05	0.03

TABLE 2. Lengthscales for $Re = 22$ and a variety of computations with varying Pe and Ri. The resolution of the numerical grid is 0.1. ($\varepsilon = 0.00046$, 0.0013, 0.0015 and 0.0014, and $\beta = 1$, 1.07, 1.03 and 3.5.)
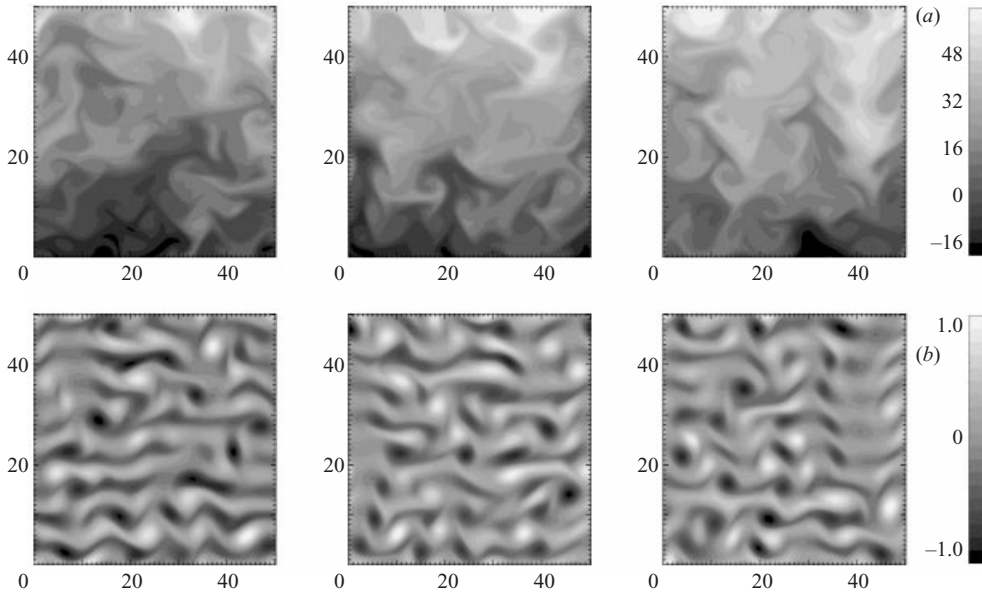

FIGURE 30. Total temperature (a) and total vorticity (b) for $Ri = 2.4 \times 10^{-4}$, $Re = 22$ and $Pe = 40$ at times 864, 1222 and 1555. A movie of the entire simulation corresponding to this figure is available at http://astro.uchicago.edu/home/web/young/linkdir/SHE004.html.

tively well-mixed background. At higher Richardson number, where stratification is stronger, these interfaces perhaps become aligned with the horizontal to form the steps of a staircase of mixed layers.

7. Conclusion

In this article we have investigated stratified Kolmogorov flows. For weakly stratified, slightly unstable, diffusive flows (with $Pe = O(1)$), the dynamics is described by an amplitude equation that reduces to the Cahn–Hilliard equation on neglecting all effects of stratification. That equation was previously derived by Sivashinsky (1985), and describes how patterns coarsen with time and gradually increase their spatial scale. The full amplitude equation contains a stratification term that halts the coarsening once the pattern reaches an intermediate spatial scale. These results illustrate
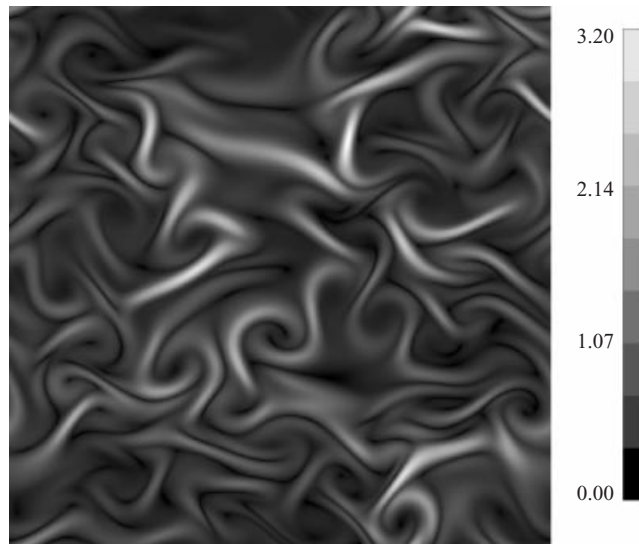
FIGURE 31. The amplitude of the final (total) temperature gradient, $|\nabla T|$, displayed on the (x, z)-plane for $Ri = 0.016$ and $Re = 22$, with $Pe = 8$.

how the inverse cascade of the Kolmogorov flow becomes arrested by stratification. Numerical simulations of the full problem confirm the predictions of the asymptotic theory, and show that the arrest of the cascade continues at higher Reynolds numbers.

In the non-diffusive limit ($Pe \gg 1$), the linear dynamics is dominated by the creation of internal boundary layers surrounding the inflection points of the basic shear flow. The boundary layers are the regions where the stabilizing effect of stratification is most effective. We explored this regime with a combination of matched asymptotic analysis and numerical simulation and found that, although stratification effects compete with the linear instability, they cannot saturate it. Instead, the stratification impedes the instability for a time, but the temperature field then becomes twisted up, removing the stabilizing gradients and allowing the instability to grow more freely. The boundary layers then thicken and grow to the scale of the basic flow whereupon large-scale patterns form. The scale of the pattern is, once again, not the largest in the domain, illustrating how the inverse cascade continues to be arrested in the non-diffusive limit. The patterns are steady at lower Reynolds number, but become aperiodic as we raise Re and drive the system harder.

Overall, we conclude that the arrest of the inverse cascade by the stabilizing stratification is a generic feature of the system, and occurs in both the horizontal and vertical directions. This signifies that we may exploit stratification to achieve statistical stationarity in numerical simulations of two-dimensional turbulence, much as friction has been utilized in the past to prevent energy from building up at the largest scales. We have not, however, driven the system into the turbulent regime, and, at best, we can only say that the flows we have simulated are chaotic.

Despite the relatively low Reynolds number, our results share some common features with simulations of turbulent flows, such as the unsteady creation and merging of vortices. Other aspects, though, are missing, notably the formation of mixed layers. It is conceivable that such layers only form when the stratification plays a dominant role in the fluid dynamics, and therefore only appear at higher Richardson numbers. Perhaps there is also a gradual reduction in vertical scale as we

raise *Ri*, so that beyond the layering regime we eventually create conditions under which motion in the vertical direction is entirely suppressed, as is commonly assumed in some geophysical contexts and to design experiments on two-dimensional fluid mechanics. Our inhibition of the inverse cascade of the Kolmogorov flow may be the first sign of this gradual reduction in scale.

Finally, we briefly compare our results to the experiments described in Batchayev *et al.* (1984) and Batchayev & Kurgansky (1986). Those experiments show that oscillations set in as a secondary instability for moderate forcing amplitude, which is consistent with our results for higher Péclet and Reynolds numbers. Qualitatively, we also obtain similar flow patterns to the experiments. However, despite these superficial similarities, we cannot quantitatively compare the theory with the experiments. This is because we consider the weakly stratified problem ($Ri < 0.01$), whereas the experimental range of Richardson number extends from 0.01 to 0.06 in Batchayev & Kurgansky (1986) and is much greater than unity in Batchayev *et al.* (1984), placing the experiments in a somewhat different parameter regime. Moreover, friction plays a crucially important role in the experiments (Batchayev *et al.* 1984; Thess 1992), and differences in boundary conditions can be significant.

Appendix A. Derivation of the amplitude equation for $Pe \sim O(1)$

With the scalings outlined in §4 and the definition $b \equiv Ri\theta/\epsilon^5 = \epsilon Ri_6\theta$ (which eases the layout of the expansion), equations (2.1) and (2.2) take the form

$$\epsilon^4\partial_\tau\nabla^2\psi - \epsilon J_\xi(\psi, \nabla^2\psi) - \epsilon\sin z(\nabla^2\psi + \psi)_\xi = \frac{1}{\sqrt{2}}(1 - \epsilon^2)\nabla^4\psi - \epsilon^6 b_\xi, \qquad (A\,1)$$

$$\epsilon^4\partial_\tau b - \epsilon J_\xi(\psi, b) - \epsilon^2 Ri_6\psi_\xi - \epsilon b_\xi \sin z = \frac{1}{Pe}\nabla^2 b, \qquad (A\,2)$$

where J_ξ is the Jacobian with respect to ξ and z, and $\nabla^2 \equiv \partial_z^2 + \epsilon^2\partial_\xi^2$. It is also helpful to take the cross-stream average of (A 1):

$$\epsilon^3\overline{\psi}_{\tau\xi\xi} - \overline{(\psi\sin z)}_{\xi\xi\xi} - \overline{(\psi_\xi\psi_z)}_{\xi\xi} = \frac{1}{\sqrt{2}}(1 - \epsilon^2)\epsilon\overline{\psi}_{\xi\xi\xi\xi} - \epsilon^3\overline{b}_\xi, \qquad (A\,3)$$

where the overline implies vertical average.

We first introduce the asymptotic sequences

$$\psi = \psi_0 + \epsilon\psi_1 + \epsilon^2\psi_2 + \epsilon^3\psi_3 + \cdots, \qquad (A\,4)$$

$$b = b_0 + \epsilon b_1 + \epsilon^2 b_2 + \epsilon^3 b_3 + \cdots, \qquad (A\,5)$$

into equations (A 1) and (A 2). We then solve (A 1) and (A 2) at different orders of ϵ with periodic boundary conditions in both ξ and z.

At $O(\epsilon^0)$

$$\psi_{0zzzz} = 0, \quad \frac{1}{Pe} b_{0zz} = 0, \tag{A 6}$$

with periodic solutions

$$\psi_0 = A(\xi, \tau), \quad b_0 = B(\xi, \tau). \tag{A 7}$$

At $O(\epsilon^1)$

$$\psi_{1zzzz} = -\sqrt{2} A_\xi \sin z, \tag{A 8}$$

$$\psi_{0z} B_\xi - \psi_{0\xi} B_z = \frac{1}{Pe} b_{1zz}; \tag{A 9}$$

the periodic solutions are

$$\psi_1 = -\sqrt{2}\, A_\xi \sin z + A_1(\xi, \tau), \quad b_1 = Pe\, B_\xi \sin z + B_1(\xi, \tau). \tag{A 10}$$

At $O(\epsilon^2)$

$$\psi_{2zzzz} = -\sqrt{2} A_{1\xi} \sin z - 2A_\xi^2 \cos z, \tag{A 11}$$

$$\frac{1}{Pe} b_{2zz} = -B_{1\xi} \sin z - (\sqrt{2} + Pe) A_\xi B_\xi \cos z - \left(\frac{Pe}{2} + \frac{1}{Pe}\right) B_{\xi\xi} - Ri_6 A_\xi + \frac{Pe}{2} B_{\xi\xi} \cos 2z. \tag{A 12}$$

The vertical average of (A 12) now provides a relation between $B(\xi, \tau)$ and $A(\xi, \tau)$:

$$\left(\frac{Pe}{2} + \frac{1}{Pe}\right) B_{\xi\xi} + Ri_6 A_\xi = 0 \quad \text{or} \quad \left(\frac{Pe}{2} + \frac{1}{Pe}\right) B_\xi + Ri_6 A = C(\tau), \tag{A 13}$$

where $C(\tau)$ is arbitrary. However, periodicity requires that $C = Ri_6 \langle A \rangle$, where the angular brackets denote horizontal average.

The periodic solution to equation (A 11) is

$$\psi_2 = -\sqrt{2} A_{1\xi} \sin z - 2A_\xi^2 \cos z + A_2(\xi, \tau). \tag{A 14}$$

At $O(\epsilon^3)$

$$\psi_{3zzzz} = \sqrt{2}(2A_\xi^3 - 3A_{\xi\xi\xi} - A_\xi - A_\xi^2) \sin z - 4\sqrt{2} A_{1\xi} A_\xi \cos z, \tag{A 15}$$

with periodic solution,

$$\psi_3 = \sqrt{2}[2A_\xi^3 - 3A_{\xi\xi\xi} - A_\xi - A_\xi^2] \sin z - 4\sqrt{2} A_{1\xi} A_\xi \cos z + A_3(\xi, \tau). \tag{A 16}$$

The cross-stream average (A 3) at $O(\epsilon^3)$ now leads to the long-wave amplitude equation quoted in the main text.

Appendix B. Long-wave theory for large Péclet number
B.1. *Regular expansion and its failure*

With the rescalings quoted in §5, the governing equations read:

$$\epsilon^4 \nabla^2 \phi_\tau - \epsilon^7 J_\xi(\phi, \nabla^2 \phi) - \epsilon \sin z (\nabla^2 \phi + \phi)_\xi = \frac{1}{\sqrt{2}}(1 - \epsilon^2)\nabla^4 \phi - \epsilon^6 Ri_5 \vartheta_\xi, \tag{B 1}$$

$$\epsilon^3 \vartheta_\tau - \epsilon^6 J_\xi(\phi, \vartheta) - \phi_\xi - \vartheta_\xi \sin z = \frac{1}{Pe_{10}} \epsilon^9 \nabla^2 \vartheta, \tag{B 2}$$

where J_ξ is the Jacobian with respect to ξ and z, and $\nabla^2 \equiv \partial_z^2 + \epsilon^2 \partial_\xi^2$. The vertical average of (B 1) provides the useful relation

$$\epsilon^3 \overline{\phi}_{\tau\xi\xi} - \overline{(\phi \sin z)}_{\xi\xi\xi} - \epsilon^6 \overline{(\phi_\xi \phi_z)}_{\xi\xi} = \frac{1}{\sqrt{2}}(1 - \epsilon^2)\epsilon\overline{\phi}_{\xi\xi\xi\xi} - \epsilon^3 Ri_5\overline{\vartheta}_\xi, \qquad (\text{B 3})$$

where the overline again denotes the vertical average.

We continue as before, and introduce the asymptotic sequences

$$\phi = \phi_0 + \epsilon\phi_1 + \cdots, \quad \vartheta = \vartheta_0 + \epsilon\vartheta_1 + \cdots. \qquad (\text{B 4})$$

It is then straightforward (and, in fact, similar to Appendix A) to derive

$$\phi_0 = A(\xi, \tau), \quad \phi_1 = -\sqrt{2}\, A_\xi \sin z + A_1(\xi, \tau), \quad \phi_2 = -\sqrt{2}\, A_{1\xi} \sin z + A_2(\xi, \tau) \quad (\text{B 5})$$

$$\phi_3 = -\sqrt{2}(3A_{\xi\xi\xi}/2 + A_\xi)\sin z + A_3(\xi, \tau). \qquad (\text{B 6})$$

With these solutions, we may expand the averaged equation (B 3). The first-order equations are automatically satisfied. At higher order, and if the expansion remained regular at this stage, we would obtain

$$A_{\tau\xi\xi} + \sqrt{2}\left(\tfrac{3}{2}A_{\xi\xi} + A\right)_{\xi\xi\xi\xi} = -\frac{Ri_5}{2\pi}\int_0^{2\pi} \vartheta_{0\xi}\mathrm{d}z. \qquad (\text{B 7})$$

However, there are problems in the derivation of this equation connected to apparent singularities in ϑ_0, as we now explicitly expose.

An analogous expansion of the heat equation leads to

$$\vartheta_0 = \frac{A}{\sin z}, \quad \vartheta_1 = \frac{A_1}{\sin z} - \sqrt{2}A_\xi, \quad \vartheta_2 = \frac{A_2}{\sin z} - \sqrt{2}A_{1\xi}, \quad \vartheta_{3\xi} = \frac{\phi_{3\xi}}{\sin z} - \frac{A_\tau}{\sin^2 z}. \quad (\text{B 8})$$

The root of the problem is evident: these solutions all diverge for $z = 0$, π and 2π. Furthermore, $\epsilon^3\vartheta_3$ breaks the ordering of the asymptotic sequence and is comparable to ϑ_0 when $z - n\pi = O(\epsilon^3)$, with $n = 0$, 1 or 2. This reflects the breakdown of the regular solution inside the thermal boundary layers which surround the inflection points of the velocity profile, and signifies that we cannot directly compute the average equation (B 7). The boundary layer scalings are

$$z \to n\pi + \epsilon^3 Z, \quad \phi(\xi, z, \tau) \to \Psi(\xi, Z, \tau), \quad \vartheta(\xi, z, \tau) \to \frac{1}{\epsilon^3}\Theta(\xi, Z, \tau). \qquad (\text{B 9})$$

Despite the apparent problems, the regular expansion furnishes a suitable solution outside the boundary layers. In other words, it provides an outer solution that must be matched to other, inner solutions valid within each boundary layer. This is how the expansion descends into matched asymptotics.

B.2. *The boundary layers*

Within each of the boundary layers the governing equations become, to leading order (which is all we shall require),

$$\partial_Z^4 \Psi^{\alpha,\beta} = O(\epsilon^2) \qquad (\text{B 10})$$

and

$$\Theta_\tau^{\alpha,\beta} \pm Z\Theta_\xi^{\alpha,\beta} - \Psi_\xi^{\alpha,\beta} - J_{\xi,Z}(\Psi^{\alpha,\beta}, \Theta^{\alpha,\beta}) = \frac{1}{P_{10}}\Theta_{ZZ}^{\alpha,\beta} + O(\epsilon^8), \qquad (\text{B 11})$$

where the Jacobian uses the inner (ξ, Z) coordinates, and the α and β superscripts are added to remind us that, in the $[0, 2\pi]$-periodic domain, there are two independent

boundary layers (surrounding $z = 0$ and π) which are indexed accordingly, and have opposite senses for the shearing of the basic flow. The motivation for the precise scaling of the Péclet number is clear from the second equation: it is chosen such that thermal diffusion neither dominates nor is negligible within the boundary layers.

We solve the first relation by taking $\Psi^{\alpha,\beta} = A(\xi, \tau)$, which automatically achieves a match between the leading-order streamfunction and temperature field of the outer and inner solutions. However, we must solve the boundary-layer heat equations as nonlinear partial differential equations:

$$\Theta_\tau^{\alpha,\beta} \pm Z\Theta_\xi^{\alpha,\beta} + A_\xi \Theta_Z^{\alpha,\beta} - A_\xi = \frac{1}{P_{10}} \Theta_{ZZ}^{\alpha,\beta}. \tag{B 12}$$

Thus far, the only reduction gained from our analysis appears to be the simplification of the streamfunction.

It remains to reconsider the averaged equation (B 7). Once we appreciate the presence of the boundary layers, it becomes feasible to avoid the apparent singularities by dividing the domain into the inner and outer regions, and using the appropriate asymptotic solutions in each (alternatively, we can construct a uniformly valid solution). That relation then becomes

$$A_{\tau\xi\xi} + \sqrt{2}\left(\frac{3}{2}A_{\xi\xi} + A\right)_{\xi\xi\xi\xi} = -\frac{Ri_5}{2\pi}\int_{-\infty}^\infty \Theta_\xi^\alpha \mathrm{d}Z - \frac{Ri_5}{2\pi}\int_{-\infty}^\infty \Theta_\xi^\beta \mathrm{d}Z, \tag{B 13}$$

where the limits arise because the two boundary layers are stretched to cover infinite intervals in the asymptotic scheme.

Two further technical details of the inner solution deserve mention. First, from (B 12), the boundary-layer temperature can be seen to have the far-field form $\Theta^{\alpha,\beta} \sim A/Z$ as $|Z| \to \infty$. This decay is sufficient to ensure that the integrals in (B 13) converge provided we take the principal value at the two limits. Second, we are interested in an initial-value problem in which a global instability grows and subsequently generates boundary layers in the temperature field. This prescribes an initial condition

$$A(\xi, 0) = A_0(\xi), \quad Z^{\alpha,\beta}(\xi, Z, 0) = 0, \tag{B 14}$$

where $A_0(\xi)$ is the small global disturbance required to stimulate the system. In practice, we take $A_0(\xi)$ to be sinusoidal, or a combination of sinusoids, but always with a point of symmetry, ξ_s, about which $A_0(\xi)$ is an even function. An important consequence of this prescription is that the system has the symmetry: $\xi \to \xi_s - \xi$, $A \to A$, $Z \to -Z$, $\Theta^{\alpha,\beta} \to -\Theta^{\alpha,\beta}$. Moreover, $\Theta^\alpha(\xi, Z, \tau) = \Theta^\beta(\xi_s - \xi, -Z, \tau) \equiv \Theta(\xi, Z, \tau)$ for all time, and we need solve only one boundary layer equation.

In summary, the long-wave instability in the weakly diffusive limit is governed by the system quoted in the main text.

REFERENCES

ARMBRUSTER, D., HEILAND, R., KOSTELICH, E. J. & NICOLAENKO, B. 1992 Phase-space analysis of bursting behaviour in Kolmogorov flow. *Physica* D **58**, 392–401 .

BALMFORTH, N. J. & CASTI, A. 1998 Convection in a slowly diffusing, weakly stratified salt field. *Lett.* A **238**, 35–42.

BALMFORTH, N. J., LLEWELLYN SMITH, S. G. & YOUNG, W. R. 2001 Disturbing vortices. *J. Fluid Mech.* **426**, 95–133.

BALMFORTH, N. J. & YOUNG, W. R. 1997 Longwave instability in shear flows. *Phys. Rev. Lett.* **79**, 4155–4159.

BATCHAYEV, A. M. 1988 Experimental investigation of supercritical Kolmogorov flow regimes on a cylindrical surface. *Izv. Acad. Sci., USSR, Atmos. Ocean. Phys.* **24**, 614–620.

BATCHAYEV, A. M., DOVZHENKO, V. A. & KURGANSKY, M. V. 1984 Simulation of shear flow in a stratified fluid. *Izv. Acad. Sci., USSR, Atmos. Ocean. Phys.* **20**, 439–442.

BATCHAYEV, A. M. & KURGANSKY, M. V. 1986 Periodic shear flow instability in a weakly stratified fluid. *Izv. Acad. Sci., USSR, Atmos. Ocean. Phys.* **22**, 1–5.

BEAUMONT, D. N. 1981 The stability of spatially periodic flows. *J. Fluid Mech.* **108**, 461–474.

BELOSHAPKIN, V., CHERNIKOV, A. A., NATENZON, N. Y. *et al.* 1989 Chaotic streamlines in pre-turbulent states. *Nature* **337**, 133–137.

BONDARENKO, N. F., GAK, M. Z. & DOLZHANSKY, F. V. 1979 Laboratory and theoretical models of plane periodic flows. *Izv. Acad. Sci., USSR, Atmos. Ocean. Phys.* **15**, 711–716.

BURGESS, J. M., BIZON, C., MCDONALD, W. D., SWIFT, J. B. & SWINNEY, H. L. 1999 Instability of the Kolmogorov flow in a soap film. *Phys. Rev. E* **15**, 715–721.

CASE, K. M. 1960 Stability of inviscid plane Couette flow. *Phys. Fluids* **3**, 143–148.

CHAPMAN, C. & PROCTOR, M. 1980 Nonlinear Rayleigh-Benard convection with poorly conducting boundaries. *J. Fluid Mech.* **101**, 759–782.

CHO, J. Y. K. & POLVANI, L. M. 1996 The emergence of jets and vortices in freely evolving, shallow-water turbulence on a sphere. *Phys. Fluids* **8**, 1531–1552.

CHURILOV, S. M. & SHUKHMAN, I. G. 1987 The nonlinear development of disturbances in a zonal shear flow. *Geophys. Astrophys. Fluid Dyn.* **38**, 145–175.

CHURILOV, S. M. & SHUKHMAN, I. G. 1996 The nonlinear critical layer resulting from the spatial or temporal evolution of weakly unstable disturbances in shear flows. *J. Fluid Mech.* **318**, 189–221.

DAVIS, P. & PELTIER, W. 1976 Resonant parallel shear instability in the stably stratified planetary boundary layer. *J. Atmos. Sci.* **33**, 1287–1300.

DRAZIN, P. & HOWARD, L. 1996 Hydrodynamic stability of parallel flow of inviscid fluid. *Adv. Appl. Mech.* **9**, 1–89.

FRIEDLANDER, S. & HOWARD, L. 1998 Instability in parallel flow revisited. *Stud. Appl. Maths* **101**, 1–21.

FRISCH, U., LEGRAS, B. & VILLONE, B. 1996 Large-scale Kolmogorov flow on the beta-plane and resonant wave interactions. *Physica* D **94**, 36–56.

GOLDSTEIN, M. E. & HULTGREN, L. S. 1988 Nonlinear spatial evolution of an externally excited instability wave in a free shear layer. *J. Fluid Mech.* **197**, 259–330.

GREEN, J. S. A. 1974 Two-dimensional turbulence near the viscous limit. *J. Fluid Mech.* **62**, 273–287.

HOWARD, L. N. 1963 Neutral curves and stability boundaries in stratified flow. *J. Fluid Mech.* **16**, 333–342.

KELLER, K. H. & VAN ATTA, C. W. 2000 An experimental investigation of the vertical temperature structures of homogeneous stratified shear turbulence. *J. Fluid Mech.* **425**, 1–29.

KURGANSKY, M. V. 1980 Instability of internal gravity waves propagating at small angles to the vertical. *Izv. Acad. Sci. USSR, Atmos. Ocean. Phys.* **16**, 758–764.

LEGRAS, B., VILLONE, B. & FRISCH, U. 1999 Dispersive stabilization of the inverse cascade for the Kolmogorov flow. *Phys. Rev. Lett.* **82**, 4440–4443.

LORENZ, E. N. 1972 Barotropic instability of Rossby wave motion. *J. Atmos. Sci.* **29**, 258–269.

MANFROI, A. & YOUNG, W. 1999 Slow evolution of zonal jets on the beta plane. *J. Atmos. Sci.* **56**, 784–800.

MCINTYRE, M. E. 1970 Diffusive destabilization of the baroclinic circular vortex. *Geophys. Fluid Dyn.* **1**, 19–57.

MCWILLIAMS, J. C. 1990 The vortices of two-dimensional turbulence. *J. Fluid Mech.* **219**, 361–385.

MESHALKIN, L. & SINAI, Y. 1961 Investigation of the stability of a stationary solution of a system of equations for the plane movement of an incompressible viscous fluid. *J. Appl. Math. Mech.* **25**, 1700.

MURAKAMI, Y. & WATANABE, Y. 1994 On unstable modes of the inviscid Kolmogorov flow. *J. Phys. Soc. Japan* **63**, 2825–2826.

NEPOMNIASHCHII, A. 1976 On stability of secondary flows of a viscous fluid in unbounded space. *J. Appl. Math. Mech.* **40**, 836–841.

NICOLAENKO, B. & SHE, Z.-S. 1989 Coherent structures, homoclinic cycles and vorticity explosions

in Navier-Stokes flows. In *Topological Fluid Dynamics* (ed. K. K. Moffatt & A. Tsinober). Cambridge University Press.

O'NEIL, T. M., WINFREY, J. H. & MALMBERG, J. H. 1971 Nonlinear interaction of a small cold beam and a plasma. *Phys. Fluids* **14**, 1204–1212.

PARK, Y.-G., WHITEHEAD, J. & GNANADESKIAN, A. 1994 Turbulent mixing in stratified fluids: layer formation and energetics. *J. Fluid Mech.* **279**, 279–311.

PLATT, N., SIROVICH, L. & FITZMAURICE, N. 1991 An investigation of chaotic Kolmogorov flows. *Phys. Fluids* A **3**, 681–696.

SHE, Z. S. 1987 Metastability and vortex pairing in the Kolmogorov flow. *Phys. Lett.* A **124**, 161–163.

SIVASHINSKY, G. 1985 Weak turbulence in periodic flows. *Physica* D **17**, 243–255.

SMYTH, W. D. & MOUM, J. H. 2000 Length scales of turbulence in stably stratified mixing layers. *Phys. Fluids* **12**, 1327–1342.

STEWARTSON, K. 1981 Marginally stable inviscid flows with critical layers. *IMA J. Appl. Maths* **27**, 133–175.

THESS, A. 1992 Instabilities in two-dimensional spatially periodic flows. Part i: Kolmogorov flow. *Phys. Fluids* A **4**, 1385–1395.

TURNER, J. S. 1985 Multicomponent convection. *Annu. Rev. Fluid Mech.* **17**, 11–44.

WARN, T. & GAUTHIER, P. 1989 Potential vorticity mixing by marginally unstable baroclinic disturbance. *Geophys. Res. Lett.* **41**, 115–131.

WARN, T. & WARN, H. 1978 The evolution of a nonlinear critical level. *Stud. Appl. Maths* **59**, 37–71.

WILLIAMS, G. P. & WILSON, R. J. 1988 The stability and genesis of Rossby vortices. *J. Atmos. Sci.* **45**, 207–241.

YOUNG, Y. 1999 On stratified Kolmogorov flow. *Woods Hole Oceanogr. Inst. Tech Rep.* 40.